Near-Field Channel Reconstruction in Sensing RIS-Assisted Wireless Communication Systems

Jiachen Tian, *Graduate Student Member, IEEE,* Yu Han, *Member, IEEE,* Shi Jin, *Fellow, IEEE,* Xiao Li, *Member, IEEE,* Jun Zhang, *Senior Member, IEEE,* and Michail Matthaiou, *Fellow, IEEE*

***Abstract*—A reconfigurable intelligent surface (RIS) with active elements is an augmented version of an RIS. By equipping all or part of RIS elements with signal processing capabilities, the channel estimation and the design of RIS phases can be further extended, yielding an improvement in the spectral efficiency (SE). In this paper, we first present a novel sensing RIS structure which is efficient for hardware implementation. Unlike partial active elements in previous structures, all elements are available to the RF chains via switches, which enables the traditional channel estimation methods and channel extrapolation to be implemented. Moreover, we make a comprehensive analysis and comparison with other RIS structures from the perspective of channel state information (CSI) acquisition. Considering the large-scale of RIS and base station (BS) array, we model the channel between the user and the RIS, the RIS and the BS using a near-field channel model. Based on the structured channel model, we propose a low-overhead channel reconstruction protocol through a parameter-extracting method, while the training overhead and complexity are also analyzed. In addition, we investigate the RIS elements' activation strategy to further reduce the training overhead. Finally, numerical results demonstrate that the proposed scheme achieves accurate channel estimation with low overhead, which can also enhance the achievable SE.**

***Index Terms*—Channel reconstruction, near-field, sensing RIS**

I. Introduction

WIRELESS communication technologies are evolving to the sixth generation (6G) and reconfigurable intelligent surfaces (RISs) have been considered as a potential underpinning technology [1], [2]. An RIS can control the electromagnetic waves flexibly and customize the electromagnetic propagation environment. By harnessing the low-cost nature of these architectures, it is convenient to deploy RISs densely to enhance the signal strength and provide controllable supplementary links. Given these attractive advantages, extensive works have studied the RIS-assisted wireless communication systems, including theoretical analysis [3], [4] and experimental measurements [5]–[7]. Moreover, extensive works have also verified the effectiveness of RISs in enhancing the spectral efficiency (SE) [8]–[11] and the ability of localization [12], [13]. However, a prerequisite to avail of these advantages above is the acquisition of channel state information (CSI), since the optimal phase design of RIS relies on accurate and timely CSI.

CSI acquisition is a difficult problem in RIS-assisted wireless communication systems since traditional RIS elements are unable to perform signal receiving and processing. Therefore, the channel between a user equipment (UE) and the RIS, and the channel between an RIS and the base station (BS) are cascaded together at the receiver. Researchers have developed extensive schemes to estimate the UE-RIS-BS channel, or the cascaded channel, in which the CSI of each RIS element is independent of the RIS phase shift [14]. However, CSI acquisition for separated channel is still a challenging problem which renders transceiver design a critical issue.

A. Related Works

Assuming that the RIS-BS channel is known a priori, [12] considered the CSI acquisition of the UE-RIS channel especially in the near field. Also, [15] employed the PARAllel FACtor (PARAFAC) decomposition to estimate the separate channels of multiple users, yet the number of BS antennas and users needs to be no less than the number of RIS elements. Based on the channel sparsity, other works tend to estimate the parameters of the separate channels through multiple measurements even if passive RISs are deployed. Moreover, [16] proposed a two-stage training strategy and an atomic norm minimization (ANM) algorithm for solving the problem based on sparsity in the angular domain.

Fortunately, the emergence of novel RIS architectures is expected to simplify the separate CSI acquisition of RIS-assisted wireless communication systems.[1] By replacing part of the passive RIS elements with active elements connected

Manuscript received xx xx, xxxx; revised xx xx, xxxx; accepted xx xx xxxx. This work was supported in part by the National Natural Science Foundation of China (NSFC) under Grants 62301148, 62261160576, 62231009, and 62071247, in part by the Natural Science Foundation of Jiangsu Province under Grant BK20230824 and BK20211511, in part by the Jiangsu Province Frontier Leading Technology Basic Research Project under Grant BK20212002, in part by the Young Elite Scientists Sponsorship Program by CAST under grant 2023QNRC001, and in part by the Fundamental Research Funds for the Central Universities under Grant 2242024RCB0006 and ZHISHAN Young Scholar Project of Southeast University. The work of M. Matthaiou was supported by the European Research Council (ERC) under the European Union's Horizon 2020 research and innovation programme (grant agreement No. 101001331). *(Corresponding author: Yu Han; Shi Jin.)*

J. Tian, Y. Han, S. Jin, and X. Li are with the National Mobile Communication Research Laboratory, Southeast University, Nanjing 210096, China (email: tianjiachen@seu.edu.cn; hanyu@seu.edu.cn; jinshi@seu.edu.cn; li_xiao@seu.edu.cn).

J. Zhang is with the Jiangsu Key Laboratory of Wireless Communications, Nanjing University of Posts and Telecommunications, Nanjing 210003, China (e-mail: zhangjun@njupt.edu.cn).

M. Matthaiou is with the Centre for Wireless Innovation (CWI), Queen's University Belfast, BT3 9DT Belfast, U.K. (e-mail: m.matthaiou@qub.ac.uk).

[1]In this paper, we only focus on the RISs with the ability of signal processing and do not consider the amplification of signals. For notational simplicity, we use the terminology hybrid RISs to represent the RISs with the ability of signal processing.

to RF chains and baseband signal processing devices, hybrid RISs are expected to receive or transmit signals. For example, [17] made an attempt and proposed a novel RIS architecture by replacing a few passive RIS elements with sensors. Then, the separate channels were estimated through extrapolation based on pilots from UE and BS, respectively. Furthermore, [18] connected the output of all RIS elements to a common RF chain and the RIS was able to perform channel estimation. Accordingly, novel training procedures and channel estimation algorithms based on hybrid RISs have been proposed. The authors in [19] considered both narrowband and wideband systems and estimated the separate channels through tensor-based algebraic methods. In [20], the separate channel estimation was executed at the RIS side, which is realized by the received pilots from the BS and UE, respectively. However, only active RIS elements are utilized for channel estimation in the aforementioned scheme. To further leverage the inherent reflection ability of the other passive RIS elements, the authors in [21] proposed an enhanced training strategy. When the active elements of the hybrid RIS receive the uplink pilots, the passive elements reflect the pilot to the BS simultaneously, which effectively reduces the training overhead. Furthermore, the sounding procedure above was further simplified in [22]. Based on channel sparsity, compressive sensing (CS) based algorithms were adopted for the UE-RIS channel and RIS-BS channel estimation, respectively, while only one uplink training procedure is required.

From another perspective, thanks to the low-cost feature, the size of an RIS can be further extended to cover the walls of buildings. Therefore, the UEs are more likely to appear in the near-field region of the RIS and the planar wavefront propagation model is no longer suitable, which calls for the near-field channel estimation schemes for the UE-RIS channel. Moreover, by considering the increase of the RIS and BS array apertures, the RIS and the BS may appear in the near-field region of each other. Note that it is convenient for the BS to control and communicate with the RIS, when the RIS is near to the BS. Extensive works have looked into the channel estimation of the near-field UE-RIS channels. In particular, [13] considered the non-stationary near-field UE-RIS channel and far-field RIS-BS channel. The channel can be reconstructed by exploiting the sparsity in the coordinate domain and through a parameter-estimation method. By using CS, [23] proposed a low-complexity channel estimation strategy with the near-field spherical wavefront assumption for extremely large-scale RIS systems. However, less works have focused on the near-field channel estimation of the RIS-BS channel. A similar scene was considered in [24], which modeled the near-field channel of two extra large-scale arrays. By exploiting the sparse transformation in the polar domain, the authors used an on-grid matching and iterative optimization method to estimate the channel.

B. Contributions

In this paper, we consider a flexible sensing RIS structure, which balances the demand of signal processing and hardware cost. Then, a near-field channel model for the UE-RIS channel and RIS-BS channel is established and a corresponding channel reconstruction scheme is proposed. Specifically, the major contributions of this paper are summarized as follows:

- *A pragmatic sensing RIS structure and comprehensive analysis of advantages in CSI acquisition*–A sensing RIS structure is considered in this paper. Driven by the new characteristics, we pursue a comprehensive comparison and analysis of different RIS structures from the perspective of CSI acquisition, including training protocols, algorithms and overhead. Compared with traditional RIS structures, the proposed sensing RIS can not only realize cascaded CSI acquisition, but can also realize accurate separate CSI acquisition at a low training overhead.
- *An efficient channel reconstruction protocol for the near-field UE-RIS channel and RIS-BS channel*–From a practical deployment perspective, the near-field channel model between the RIS and the BS, as well as the RIS and the UE are considered, respectively. Based on this channel model, an efficient separate channel reconstruction protocol is proposed. In this protocol, an enhanced near-field Newtonized orthogonal matching pursuit (NOMP) estimator is extended from [25] to extract the near-field multipath components in both the UE-RIS channel and RIS-BS channel.
- *Theoretical analysis of different RIS patterns for CSI extrapolation*–Due to the limited number of RF chains available for the RIS elements, only signals incident on a portion of RIS elements are available for signal processing when performing channel estimation, and the whole CSI is obtained through extrapolation. Therefore, the influence of different RIS pattern configurations is investigated. Specifically, we compare four RIS pattern configurations from the perspective of radiation pattern and parameter estimation accuracy, respectively, and illustrate the superiority of the random strategy scheme.

C. Organization and Notations

The rest of this paper is organized as follows: Section II describes the system layout and the proposed sensing RIS structure. The proposed channel reconstruction scheme is introduced in Section III. The strategy for RIS elements' activation is illustrated in Section IV. In Section V, numerical results are presented and discussed. Finally, the conclusions are given in Section VI.

Notations–Vectors and matrices are denoted by bold lowercase and uppercase letters, respectively. The superscripts $(\cdot)^\top$, $(\cdot)^{\mathsf{H}}$ and $(\cdot)^\dagger$ represent the transpose, conjugate transpose and pseudo inverse, respectively. The operator $\Re\{\cdot\}$ takes the real part of a complex number; $[\mathbf{A}]_{m,n}$, $[\mathbf{A}]_{:,q}$ and $[\mathbf{b}]_{i:j}$ stand for the element in the m-th row and n-th column of matrix $\mathbf{A}$, the elements in the q-th column of matrix $\mathbf{A}$, and the i-th to j-th elements in vector $\mathbf{b}$, respectively; $\mathbb{E}\{\cdot\}$ is the expectation operation; $\mathrm{diag}(\cdot)$ and $\mathrm{blkdiag}(\cdot)$ are a diagonal matrix and a block diagonal matrix, respectively. The absolute value of a complex number a is $|a|$, $\|\cdot\|_1$ represents the ℓ_1-norm, $\|\cdot\|$ and $\|\cdot\|_F$ represent the ℓ_2-norm and Frobenius-norm of a vector and a matrix, respectively. The integer ceiling is denoted as

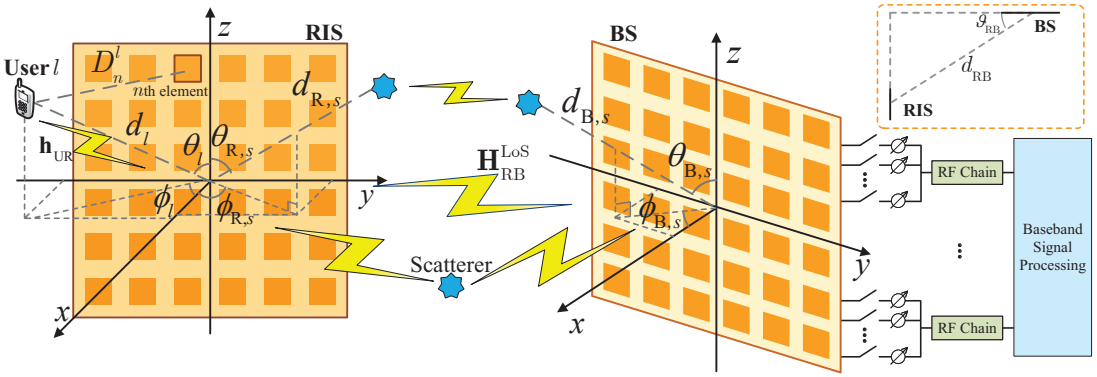

Fig. 1. Illustration of the coordinate system.

$\lceil\cdot\rceil$ and $\mathrm{vec}(\cdot)$ is the vectorization. Finally, $\mathcal{U}$ and $\mathcal{CN}$ are used to indicate the uniform distribution and the complex Gaussian distribution, respectively.

II. System Model

A. Channel Model

An RIS-assisted wireless communication system working in time division duplex (TDD) mode is considered. The BS array and the RIS both deploy a uniform planar array (UPA), and are equipped with half-wavelength spaced, i.e. $d_a = \frac{\lambda}{2}$, N_{B} and N_{R} elements, respectively, satisfying $N_{\mathrm{R}} = N_{\mathrm{R}v}N_{\mathrm{R}h}$ and $N_{\mathrm{B}} = N_{\mathrm{B}v}N_{\mathrm{B}h}$. As shown in Fig. 1, a subarray-based hybrid beamforming (BF) structure with switches is employed at the BS, while the number of RF chains is $N_{\mathrm{RF,B}}$. Each RF chain is connected with $N_{\mathrm{B}}/N_{\mathrm{RF,B}}$ elements. This HBF structure is an enhanced version of the traditional subarray-based HBF structure derived from [26], which avails of higher flexibility for channel extrapolation and lower hardware overhead than the fully-connected HBF structure [27]. The RIS is equipped with $N_{\mathrm{RF,R}}$ RF chains for signal processing. We only consider one single-antenna UE because different UEs can be separated by orthogonal pilots, whilst the channel estimations of different users are identical and independent of each other.

Since the increased apertures of the RIS and the BS array increase the range of near field, the traditional planar wavefront model is no longer suitable. Assuming that the channel between the BS and the UE is blocked, we model the UE-RIS channel and the RIS-BS channel based on the finite-dimensional channel model [28] in the near field, where the parameters of each path are assumed to be constant during the channel coherence time. As shown in Fig. 1, we establish coordinate systems for the RIS and the BS, respectively, and we take the RIS as an example to illustrate. The RIS is fixed on the yz-plane and the Cartesian coordinates of the n-th RIS element are $\mathbf{c}_n = [0, y_{n_h}, z_{n_v}]^\top$, where $y_{n_h} = (n_h - \frac{N_{\mathrm{R}h}+1}{2})d_a, n_h = 1, ..., N_{\mathrm{R}h}$, $z_{n_v} = (n_v - \frac{N_{\mathrm{R}v}+1}{2})d_a, n_v = 1, ..., N_{\mathrm{R}v}$ and $n = (n_h - 1)N_{\mathrm{R}v} + n_v$. Similarly, the coordinate system of the BS can be obtained following the same approach.

We first consider the model of the UE-RIS channel. We also assume that the signal sent by the UE arrives at the RIS along the line-of-sight (LoS) path or is reflected by multiple scatterers, and we only focus on the last-hop scatterers of the NLoS paths. Moreover, the UE antenna is regarded to be equivalent to the scatterer for the LoS path. Then, the location of scatterer l w.r.t the RIS can be denoted in the polar coordinate system as $\mathbf{p}_l = [d_l, \theta_l, \phi_l]^\top$, where d_l is the distance between the scatterer l and the origin of the coordinate system, while θ_l and ϕ_l represent the physical angles in the elevation and azimuth, respectively, denoted as $\Upsilon_{\mathrm{R},l} = \{d_l, \theta_l, \phi_l\}$. Notably, the parameters are assumed to be uniformly distributed in a given range, i.e. $d_l \sim \mathcal{U}[d_{\min}, d_{\max}]$, $\theta_l \sim \mathcal{U}[\theta_{\min}, \theta_{\max}]$ and $\phi_l \sim \mathcal{U}[\phi_{\min}, \phi_{\max}]$, while $\mathbf{p}_l$ can also be converted to Cartesian coordinates as $\mathbf{c}_l = d_l[\sin\theta_l\cos\phi_l, \sin\theta_l\sin\phi_l, \cos\theta_l]^\top$.

Assuming the channel power is concentrated on L resolvable paths and the large-scale pathloss is equal across all RIS elements, the near-field channel from the UE to the RIS is

$$\mathbf{h}_{\mathrm{UR}} = \frac{1}{\sqrt{L}}\sum_{l=1}^{L} g_l \mathbf{b}_{\mathrm{R}}(d_l, \theta_l, \phi_l), \tag{1}$$

where g_l is the complex gain of the l-th path, $\mathbf{b}_{\mathrm{R}}(d_l, \theta_l, \phi_l) \in \mathbb{C}^{N_{\mathrm{R}}\times 1}$ is the array steering vector, which can be derived based on the spherical wavefront model as

$$\mathbf{b}_{\mathrm{R}}(d_l, \theta_l, \phi_l) = \left[e^{-\jmath 2\pi D_1^l}, ..., e^{-\jmath 2\pi D_n^l}, ..., e^{-\jmath 2\pi D_{N_{\mathrm{R}}}^l}\right]^\top, \tag{2}$$

where D_n^l is the distance[2] between the scatterer l and the n-th RIS element, satisfying

$$D_n^l = \sqrt{d_l^2 - 2d_l(y_{n_h}\sin\theta_l\sin\phi_l + z_{n_v}\cos\theta_l) + y_{n_h}^2 + z_{n_v}^2}. \tag{3}$$

Note that we assume that the scatterers are in the Fresnel region [29] of the BS array and the RIS, therefore the unequal large-scale fading of different elements can be ignored. The channel between the RIS and BS can be modeled based on the near-field channel model, and contains two components:

$$\mathbf{H}_{\mathrm{RB}} = \mathbf{H}_{\mathrm{RB}}^{\mathrm{LoS}} + \mathbf{H}_{\mathrm{RB}}^{\mathrm{NLoS}}, \tag{4}$$

where $\mathbf{H}_{\mathrm{RB}}^{\mathrm{LoS}} \in \mathbb{C}^{N_{\mathrm{R}}\times N_{\mathrm{B}}}$ and $\mathbf{H}_{\mathrm{RB}}^{\mathrm{NLoS}} \in \mathbb{C}^{N_{\mathrm{R}}\times N_{\mathrm{B}}}$ are the LoS path and NLoS multipath matrices of the RIS-BS channel, respectively. The LoS matrix is determined by the distances

[2]Note that all the distance-related variables in the paper are normalized by the wavelength λ.

between the BS elements and RIS elements, whose (n_{R}-th, n_{B}-th) element is denoted as

$$\left[\mathbf{H}_{\mathrm{RB}}^{\mathrm{LoS}}\right]_{n_{\mathrm{R}},n_{\mathrm{B}}} = e^{-\jmath 2\pi D_{n_{\mathrm{R}},n_{\mathrm{B}}}}, \tag{5}$$

where $D_{n_{\mathrm{R}},n_{\mathrm{B}}}$ is the distance between the n_{R}-th RIS element and the n_{B}-th BS element. As shown in Fig. 1, the geometric relationship between the RIS and BS is determined by d_{RB} and ϑ_{RB}. Then, the LoS path of the RIS-BS channel can be calculated. Assuming that there exist S NLoS paths and only focusing on the first-hop and last-hop of each path, the $\mathbf{H}_{\mathrm{RB}}^{\mathrm{NLoS}}$ can also be modeled based on the finite-dimensional channel model [24]

$$\mathbf{H}_{\mathrm{RB}}^{\mathrm{NLoS}} = \frac{1}{\sqrt{S}}\sum_{s=1}^{S} g_s \mathbf{b}_{\mathrm{R}}(d_{\mathrm{R},s},\theta_{\mathrm{R},s},\phi_{\mathrm{R},s})\mathbf{b}_{\mathrm{B}}^{\mathsf{H}}(d_{\mathrm{B},s},\theta_{\mathrm{B},s},\phi_{\mathrm{B},s}), \tag{6}$$

where $g_{\mathrm{RB},s}$ is the complex gain of the s-th path, $\mathbf{b}_{\mathrm{R}}(\cdot) \in \mathbb{C}^{N_{\mathrm{R}}\times 1}$ and $\mathbf{b}_{\mathrm{B}}(\cdot) \in \mathbb{C}^{N_{\mathrm{B}}\times 1}$ are the near-field steering vectors of RIS and BS, respectively, while the parameter sets $\Upsilon_{\mathrm{R},s} = \{d_{\mathrm{R},s},\theta_{\mathrm{R},s},\phi_{\mathrm{R},s}\}$ and $\Upsilon_{\mathrm{B},s} = \{d_{\mathrm{B},s},\theta_{\mathrm{B},s},\phi_{\mathrm{B},s}\}$ are the parameters of the first and last hop in s-th path w.r.t. the RIS and BS, respectively. Notably, the RIS-BS channel from the RIS to the BS, i.e., $\mathbf{H}_{\mathrm{BR}}^{\mathrm{LoS}}$ and $\mathbf{H}_{\mathrm{BR}}^{\mathrm{NLoS}}$, can be obtained by switching the subscripts R and B.

B. CSI acquisition for different RIS structures

CSI acquisition is a formidable challenge in RIS-assisted wireless communication systems, which can be divided into cascaded CSI acquisition and separate CSI acquisition. In this part, we detail the general CSI acquisition procedure and linear algorithms for different RIS structures, especially the proposed sensing RIS structure.

1) Traditional Passive RIS: The passive RIS usually refers to an RIS equipped with neither amplifiers nor RF chains for signal processing. Therefore, the separate channels $\mathbf{h}_{\mathrm{UR}}$ and $\mathbf{H}_{\mathrm{RB}}$ are cascaded through the RIS phase matrix $\mathbf{\Theta} \in \mathbb{C}^{N_{\mathrm{R}}\times N_{\mathrm{R}}}$ and the channel estimation is executed at the BS side or the UE side [14], [30]. Considering the scenario with a single UE and uplink training, the signal received by the BS at time instance t is

$$\mathbf{y}_t = \sqrt{P_{\mathrm{U}}}\mathbf{H}_{\mathrm{BR}}\mathbf{\Theta}_t\mathbf{h}_{\mathrm{UR}}x + \mathbf{n}_t = \sqrt{P_{\mathrm{U}}}\mathbf{G}\boldsymbol{\vartheta}_t x + \mathbf{n}_t, \tag{7}$$

where $\mathbf{G} \triangleq \mathbf{H}_{\mathrm{RB}}\,\mathrm{diag}(\mathbf{h}_{\mathrm{UR}})$ is the cascaded channel, $\boldsymbol{\vartheta}_t = \mathrm{diag}(\mathbf{\Theta}_t)$ is the phase vector of the RIS, and $\mathbf{n} \sim \mathcal{CN}(\mathbf{0},\sigma^2\mathbf{I})$ is the additive white Gaussian noise (AWGN). By switching $\boldsymbol{\vartheta}_t$ over T time instances and regarding it as the pilot signal, the least-square (LS) estimate of the cascaded channel is

$$\hat{\mathbf{G}}_{\mathrm{LS}} = \frac{1}{\sqrt{P_{\mathrm{U}}}}\mathbf{Y}\mathbf{P}^{\dagger}, \tag{8}$$

where $\mathbf{Y} = [\mathbf{y}_1,...,\mathbf{y}_T] \in \mathbb{C}^{N_{\mathrm{B}}\times T}$ and $\mathbf{P} = [\boldsymbol{\vartheta}_1,...,\boldsymbol{\vartheta}_T] \in \mathbb{C}^{N_{\mathrm{R}}\times T}$. The linear minimum mean square error (LMMSE) estimate is

$$\hat{\mathbf{G}}_{\mathrm{LMMSE}} = \mathbf{R}_{\mathrm{G}}\left(\mathbf{R}_{\mathrm{G}} + \frac{\sigma_n^2}{P_{\mathrm{U}}}\mathbf{I}\right)^{-1}\hat{\mathbf{G}}_{\mathrm{LS}}, \tag{9}$$

where $\mathbf{R}_{\mathrm{G}}$ is the covariance matrix of $\mathbf{G}$. Note that the traditional linear algorithms require that $\mathbf{P}$ is a full-rank matrix, which means that the training overhead should be no less than N_{R}.

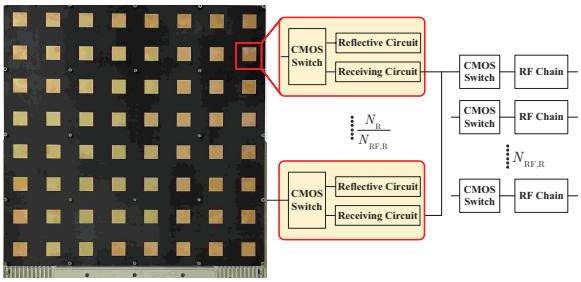

Fig. 2. Illustration of the proposed sensing RIS structure with an 8×8 dimension. A larger aperture can be realized through the placement of more tiles together.

Regarding the separate CSI acquisition, many works have proposed advanced algorithms to solve the problem [12], [15], [16]. However, these works suffer from some fundamental limitations, such as high computational complexity, high training overhead and strong assumption on number of RIS elements.

2) Semi-passive RIS: The concept of semi-passive RISs refers to RISs with $N_{\mathrm{R}}^{\mathrm{act}}$ ($N_{\mathrm{R}}^{\mathrm{act}} < N_{\mathrm{R}}$) sensors[3] which replace the reflective passive elements and are connected to RF chains. Since the cascaded CSI acquisition is similar to the traditional passive RISs, we focus more on the separate CSI acquisition. Based on these sensors, the RIS can actively sense the UE-RIS channel and RIS-BS channel. Assuming uplink training, the signal received by the sensors at the RIS is

$$\mathbf{y}_{\mathrm{R}} = \sqrt{P_{\mathrm{U}}}\grave{\mathbf{h}}_{\mathrm{UR}} + \mathbf{n}, \tag{10}$$

where $\grave{\mathbf{h}}_{\mathrm{UR}} \in \mathbb{C}^{N_{\mathrm{R}}^{\mathrm{act}}\times 1}$ is the channel between the UE and the sensors of RIS, and $\mathbf{n}$ is the noise term. Regarding the structured channel, the full-dimensional UE-RIS channel and RIS-BS channel can be extrapolated from these sensors through a parameter-estimation based scheme. The estimated channel gains $\{\hat{g}_l\}_{l=1}^{L}$ and parameter sets (such as angles, distances, etc) $\{\hat{\Psi}_l\}_{l=1}^{L}$ for L paths can be obtained by solving the following problem

$$\{\hat{g}_l,\hat{\Psi}_l\}_{l=1}^{\hat{L}} = \arg\min_{g,\Psi} \|\mathbf{y}_{\mathrm{R}} - \sqrt{P_{\mathrm{U}}}\grave{\mathbf{h}}_{\mathrm{UR}}(g,\Psi)\|^2. \tag{11}$$

However, these RIS structures fail to estimate the non-structured channel due to the lack of full-dimensional sensing capabilities. At the same time, linear channel estimation schemes are available only if the partial channel $\grave{\mathbf{h}}_{\mathrm{UR}}$ is correlated with the full-dimensional channel $\mathbf{h}_{\mathrm{UR}}$ [31].

3) Proposed Sensing RIS: We now propose a practical switch-based sensing RIS structure, which is shown in Fig. 2. Each element is connected with two parts: reflection circuit and receiving circuit, via a CMOS switch. That is to say, each RIS element has two modes: the reflection mode and the receiving mode. In the *reflection mode*, the RIS element is able to reflect the incident signal based on the configured phase shift. In the *receiving mode*, the incident signal of the RIS element is

[3]In this paper, the term "sensor" generally refers to the devices with only signal sensing and receiving capabilities, whilst the ability to transmit signals is not considered for the RIS.

received and then sent to the RF chain for subsequent baseband signal processing. Due to the consideration of hardware cost, only $N_{\mathrm{RF,R}}$ RF chains are deployed and $N_{\mathrm{R}}/N_{\mathrm{RF,R}}$ RIS elements are connected with the same RF chain by a CMOS switch. Therefore, only $N_{\mathrm{RF,R}}$ signals are received for CSI acquisition in the same time instance. Compared with semi-passive RIS structures, the outstanding characteristic of the proposed sensing RIS is that all elements are able to receive signals by switching, which makes linear channel estimation schemes applicable. Note that such enhancement does not lead to high power consumption and hardware cost. The additional power consumption introduced by the RF switches is approximately 240 mW for the proposed RIS structure with 8×8 elements shown in Fig. 2 [32]. We point out that the ability to transmit signals is not considered for the proposed RIS structure, while low-cost RF chains only for receiving purposes can be deployed at the RIS to further reduce the hardware cost.

When performing linear channel estimation for non-structured channels, we stack the received signals among $T = N_{\mathrm{R}}/N_{\mathrm{RF,R}}$ time instances as

$$\mathbf{y}_{\mathrm{R}} = \begin{bmatrix} \mathbf{y}_{\mathrm{R}}^{(1)} \\ \vdots \\ \mathbf{y}_{\mathrm{R}}^{(T)} \end{bmatrix} = \sqrt{P_{\mathrm{U}}} \begin{bmatrix} \grave{\mathbf{h}}_{\mathrm{UR}}^{(1)} \\ \vdots \\ \grave{\mathbf{h}}_{\mathrm{UR}}^{(T)} \end{bmatrix} + \mathbf{n}, \tag{12}$$

where $\grave{\mathbf{h}}_{\mathrm{UR}}^{(t)}, t = 1, ..., T$ represents the channel between the UE and RIS elements active at time instance t. To cover the full RIS, note that the active RIS elements in time instance t should not be duplicated. Based on (12), the estimated UE-RIS channel $\hat{\mathbf{h}}_{\mathrm{UR}}$ can be obtained through linear channel estimation schemes, such as LS and LMMSE. The RIS-BS channel can be estimated at the RIS by receiving downlink pilots. We assume that each downlink pilot $\mathbf{x}_n \in \mathbb{C}^{N_{\mathrm{B}} \times 1}$ spans T time instances. Stacking the received pilots among N_{B} pilots at the RIS, we obtain

$$\mathbf{Y}_{\mathrm{R}} = \begin{bmatrix} \grave{\mathbf{H}}_{\mathrm{RB}}^{(1)} \\ \vdots \\ \grave{\mathbf{H}}_{\mathrm{RB}}^{(T)} \end{bmatrix} \left[\mathbf{x}_1, ..., \mathbf{x}_{n_{\mathrm{B}}}, ..., \mathbf{x}_{N_{\mathrm{B}}} \right] + \mathbf{N}, \tag{13}$$

where $\grave{\mathbf{H}}_{\mathrm{RB}}^{(t)} \in \mathbb{C}^{N_{\mathrm{R}}^{\mathrm{act}} \times N_{\mathrm{B}}}, t = 1, ..., T$ is the channel between $N_{\mathrm{R}}^{\mathrm{act}}$ RIS elements and BS antennas, and $\mathbf{N}$ is the AWGN. In accordance with (13), linear channel estimation can be performed to obtain $\hat{\mathbf{H}}_{\mathrm{RB}}$ and the training overhead is $N_{\mathrm{B}} N_{\mathrm{R}}/N_{\mathrm{RF,R}}$.

In Table I, the requirements of CSI acquisition for different RIS structures are summarized, while the training overhead of different RIS structures can be found in Section III-D. Based on the analysis above, it can be concluded that the proposed sensing RIS shows superiority in CSI acquisition, especially separate CSI acquisition. Not only the parameterized channel reconstruction algorithms are applicable to the structured channel, but also linear channel estimation schemes are available for the unstructured channel.

TABLE I
REQUIREMENTS OF CSI ACQUISITION METHODS FOR DIFFERENT CATEGORIES OF RISS

CSI acquisition	passive RIS	semi-passive RIS	sensing RIS
cascaded CSI	preferable	not necessary	not necessary
separate CSI	conditional	conditional	**available**

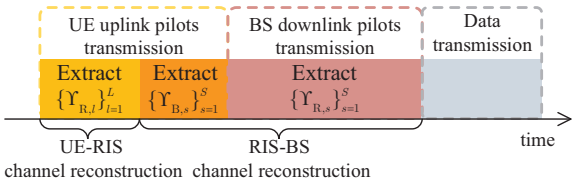

Fig. 3. Proposed transmission protocol.

III. Proposed Channel Reconstruction Scheme

Although separate CSI is available through traditional linear channel estimation methods for the proposed sensing RIS structure, the training overhead is still unaffordable. Fortunately, thanks to the structured channel model, the CSI acquisition can be implemented through a parameter-estimation method. Therefore, a low-overhead CSI acquisition scheme should be considered, whilst the flexibility of RIS structure and the accuracy of reconstructed CSI are also of great importance.

In this section, we first introduce the proposed protocol of the channel reconstruction scheme. Afterwards, we illustrate the proposed near-field NOMP-based channel reconstruction scheme for the UE-RIS channel and RIS-BS channel. Finally, we make a comparison of the training overhead with other schemes and analyze the computational complexity to evaluate the proposed scheme. Compared with other channel estimation schemes based on traditional RIS structures, the proposed channel reconstruction scheme is proven to entail low training overhead as well as to yield excellent accuracy.

A. Training Protocol

It is rational to assume that the LoS path in the RIS-BS channel is constant because of the fixed positions of the BS and the RIS [33]. Therefore, the estimation of the LoS path in the RIS-BS channel can be carried out via measurement due to the power dominance of the LoS path, or via mathematical calculations based on the geometric relationship between the RIS and the BS. Hence, we now focus on the estimation of the UE-RIS channel and of only the NLoS paths in the RIS-BS channel.

As shown in Fig. 3, the CSI of the UE-RIS channel and that of the RIS-BS channel are obtained through an uplink training procedure and a downlink training procedure, respectively. In the uplink training, the parameters of the UE-RIS channel and partial parameters of the RIS-BS channel are estimated, while in the downlink training, the remaining parameters of the RIS-BS channel are obtained.

B. UE-RIS Channel Reconstruction

The UE sends uplink pilots to the RIS. Some RIS elements are active and receive the signal, while the other passive

elements reflect the signal to the BS. In time instance t, assuming that the uplink pilot sent by the UE is x, the signal received by the active elements of the RIS is

$$\mathbf{y}_{\mathrm{UR},t} = \sqrt{P_{\mathrm{U}}}\mathbf{W}_{\mathrm{R},t}^{\mathrm{UL}}\mathbf{h}_{\mathrm{UR}}x + \mathbf{n}_{\mathrm{UR},t}, \tag{14}$$

where P_{U} is the transmit power of the UE, $\mathbf{W}_{\mathrm{R},t}^{\mathrm{UL}} \in \{0,1\}^{N_{\mathrm{R},t}^{\mathrm{UL}} \times N_{\mathrm{R}}}$ is the element selection matrix that selects $N_{\mathrm{R},t}^{\mathrm{UL}}$ active elements from N_{R} elements, and $\mathbf{n}_{\mathrm{R},t}$ is the AWGN, satisfying $\mathbf{n}_{\mathrm{R},t} \sim \mathcal{CN}(\mathbf{0}, \sigma_n^2\mathbf{I})$. Note that the number of active RIS elements in one time instance should be no more than the number of RF chains, i.e. $N_{\mathrm{R},t}^{\mathrm{UL}} \leq N_{\mathrm{RF,R}}$. Assuming that $N_{\mathrm{R},t}^{\mathrm{UL}} = N_{\mathrm{RF,R}}$ elements are active in each time instance and $N_{\mathrm{R}}^{\mathrm{UL}}$ active elements are needed totally, then the stacked signal model among $T_{\mathrm{U}} = \lceil N_{\mathrm{R}}^{\mathrm{UL}}/N_{\mathrm{RF,R}} \rceil$ time instances is

$$\mathbf{y}_{\mathrm{UR}} = \sqrt{P_{\mathrm{U}}}\mathbf{W}_{\mathrm{R}}^{\mathrm{UL}}\mathbf{h}_{\mathrm{UR}}x + \mathbf{n}_{\mathrm{UR}}, \tag{15}$$

where $\mathbf{W}_{\mathrm{R}}^{\mathrm{UL}} = \left[\mathbf{W}_{\mathrm{R},1}^{\mathrm{UL}\top}, ..., \mathbf{W}_{\mathrm{R},T_{\mathrm{U}}}^{\mathrm{UL}\top}\right]^{\top}$ is the stacked activation matrix, $\mathbf{y}_{\mathrm{UR}} = \left[\mathbf{y}_{\mathrm{UR},1}^{\top}, ..., \mathbf{y}_{\mathrm{UR},T_{\mathrm{U}}}^{\top}\right]^{\top}$ and $\mathbf{n}_{\mathrm{UR}} = \left[\mathbf{n}_{\mathrm{UR},1}^{\top}, ..., \mathbf{n}_{\mathrm{UR},T_{\mathrm{U}}}^{\top}\right]^{\top}$ are the stacked received signal vectors and noise vectors, respectively.

By leveraging the parametric channel model, the channel can be reconstructed through an iterative way, and the parameters of one path are extracted in each iteration. Assuming that an all-one pilot is sent by the UE, the UE-RIS channel reconstruction can be formulated as the following problem

$$\{\hat{g}_l, \hat{d}_l, \hat{\theta}_l, \hat{\phi}_l\}_{l=1}^{\hat{L}} = \underset{\{g,d,\theta,\phi\}}{\arg\min} \|\mathbf{y}_{\mathrm{UR}} - \sqrt{P_{\mathrm{U}}}\mathbf{W}_{\mathrm{R}}^{\mathrm{UL}}\mathbf{h}_{\mathrm{UR}}\|^2. \tag{16}$$

At each iteration, a new quaternary parameter set $(\hat{g}, \hat{d}, \hat{\theta}, \hat{\phi})$ is detected, and then the estimated path is removed from the received pilot. At the end of the $(i-1)$-th iteration, the residual signal can be denoted as

$$\mathbf{y}_{\mathrm{UR},i}^{\mathrm{res}} = \mathbf{y}_{\mathrm{UR}} - \sum_{l=0}^{i-1} \hat{g}_l \grave{\mathbf{b}}(\hat{d}_l, \hat{\theta}_l, \hat{\phi}_l), \tag{17}$$

where $\grave{\mathbf{b}}(\hat{d}_l, \hat{\theta}_l, \hat{\phi}_l) = \sqrt{P_{\mathrm{U}}}\mathbf{W}_{\mathrm{R}}^{\mathrm{UL}}\mathbf{b}(\hat{d}_l, \hat{\theta}_l, \hat{\phi}_l)$ is the equivalent steering vector, and $\{\hat{d}_l, \hat{\theta}_l, \hat{\phi}_l\}_{l=0}^{i-1}$ represents the quaternary parameter set estimated in the previous $(i-1)$ iterations.

The near-field NOMP algorithm initially checks whether the iterations can be terminated. If all the paths have been estimated, or only if the noise remains in the residual, the algorithm stops. Here, we design the stopping criterion as $\|\mathbf{y}_{\mathrm{UR},i}^{\mathrm{res}}\|^2 < \xi$, where the parameter ξ is defined as $\xi = N_{\mathrm{R}}^{\mathrm{UL}}\sigma_n^2$ [34].

In the i-th iteration, a new quaternary parameter set $(\hat{g}_i, \hat{d}_i, \hat{\theta}_i, \hat{\phi}_i)$ can be obtained by minimizing the residual power as

$$\begin{aligned}(\hat{g}_i, \hat{d}_i, \hat{\theta}_i, \hat{\phi}_i) &= \underset{g,d,\theta,\phi}{\arg\min} \|\mathbf{y}_{\mathrm{UR},i}^{\mathrm{res}} - g\grave{\mathbf{b}}(d,\theta,\phi)\|^2 \\ &= \underset{g,d,\theta,\phi}{\arg\max}\, S_i(g,d,\theta,\phi),\end{aligned} \tag{18}$$

where $S_i(g,d,\theta,\phi)$ is defined as follows

$$S_i(g,d,\theta,\phi) \triangleq 2\Re\{\mathbf{y}_{\mathrm{UR},i}^{\mathrm{res}\,\mathsf{H}} g\grave{\mathbf{b}}(d,\theta,\phi)\} - |g|^2\|\grave{\mathbf{b}}(d,\theta,\phi)\|^2. \tag{19}$$

The procedure of finding the desired path i is described below.

1) Step 1: The coarse estimates of path i can be obtained by searching for a coordinate-based codebook $\Omega_{\mathrm{R}}^{\mathrm{UL}}$. Taking the derivative of (19) w.r.t. g and equating it to zero, we can get

$$g_i = \frac{\grave{\mathbf{b}}^{\mathsf{H}}(d,\theta,\phi)\mathbf{y}_{\mathrm{UR},i}^{\mathrm{res}}}{\|\grave{\mathbf{b}}(d,\theta,\phi)\|^2}. \tag{20}$$

Subsituting (20) to (19), the coarse estimates can be obtained by solving the following problem

$$(\tilde{d}_i, \tilde{\theta}_i, \tilde{\phi}_i) = \underset{(d,\theta,\phi)\in\Omega_{\mathrm{R}}^{\mathrm{UL}}}{\arg\max} \frac{|\grave{\mathbf{b}}^{\mathsf{H}}(d,\theta,\phi)\mathbf{y}_{\mathrm{UR},i}^{\mathrm{res}}|^2}{\|\grave{\mathbf{b}}(d,\theta,\phi)\|^2}. \tag{21}$$

The codebook $\Omega_{\mathrm{R}}^{\mathrm{UL}}$ is defined based on the characteristics of the spherical wavefront as

$$\begin{aligned}\Omega_{\mathrm{R}}^{\mathrm{UL}} = \{(d,\theta,\phi) \mid d = d_{\min}^{\frac{N_d-n_d}{N_d}} d_{\max}^{\frac{n_d}{N_d}}, n_d = 1,\ldots,N_d,\\ \theta = \theta_{\min},\ldots,\theta_{\min}+n_\theta\Delta\theta,\ldots,\theta_{\max}, n_\theta = 1,\ldots,N_\theta,\\ \phi = \phi_{\min},\ldots,\phi_{\min}+n_\phi\Delta\phi,\ldots,\phi_{\max}, n_\phi = 1,\ldots,N_\phi\},\end{aligned} \tag{22}$$

where N_d, N_θ and N_ϕ are the dimensions of the codebook in distance and angle, respectively, while $\Delta\theta$ and $\Delta\phi$ are the steps of elevation angle and azimuth angle, respectively. Accordingly, the coarse estimate of g_i, denoted as $\tilde{g}_i$, is obtained by applying $\tilde{d}_i$, $\tilde{\theta}_i$ and $\tilde{\phi}_i$ in (20) and the residual is updated by the following:

$$\mathbf{y}_{\mathrm{UR},i}^{\mathrm{res}\,\prime} = \mathbf{y}_{\mathrm{UR},i}^{\mathrm{res}} - \tilde{g}_i\grave{\mathbf{b}}(\tilde{d}_i, \tilde{\theta}_i, \tilde{\phi}_i). \tag{23}$$

2) Step 2: Next, the coarse estimates are refined by Newton refinement of the NOMP algorithm. It is expressed as

$$\begin{bmatrix}\tilde{d}_i' \\ \tilde{\theta}_i' \\ \tilde{\phi}_i'\end{bmatrix} = \begin{bmatrix}\tilde{d}_i \\ \tilde{\theta}_i \\ \tilde{\phi}_i\end{bmatrix} - \ddot{\mathbf{S}}_i^{-1}\left(\tilde{g}_i, \tilde{d}_i, \tilde{\theta}_i, \tilde{\phi}_i\right)\dot{\mathbf{S}}_i\left(\tilde{g}_i, \tilde{d}_i, \tilde{\theta}_i, \tilde{\phi}_i\right), \tag{24}$$

where $\dot{\mathbf{S}}$ and $\ddot{\mathbf{S}}$ contain the first- and second-order partial derivatives, respectively, denoted as

$$\dot{\mathbf{S}}_i(d,\theta,\phi) = \begin{bmatrix}\frac{\partial S_i}{\partial d} \\ \frac{\partial S_i}{\partial \theta} \\ \frac{\partial S_i}{\partial \phi}\end{bmatrix}, \ddot{\mathbf{S}}_i(d,\theta,\phi) = \begin{bmatrix}\frac{\partial^2 S_i}{\partial d^2} & \frac{\partial^2 S_i}{\partial d\partial\theta} & \frac{\partial^2 S_i}{\partial d\partial\phi} \\ \frac{\partial^2 S_i}{\partial\theta\partial d} & \frac{\partial^2 S_i}{\partial\theta^2} & \frac{\partial^2 S_i}{\partial\theta\partial\phi} \\ \frac{\partial^2 S_i}{\partial\phi\partial d} & \frac{\partial^2 S_i}{\partial\phi\partial\theta} & \frac{\partial^2 S_i}{\partial\phi^2}\end{bmatrix}. \tag{25}$$

Simultaneously, the residual in function S_i becomes $\mathbf{y}_{\mathrm{UR},i}^{\mathrm{res}\,\prime}$. The refinement step is effective only if the residual power decreases. Otherwise, the previous coarse estimates should be remained. The Newton refine step is repeated for R_s times to obtain the most accurate estimates. Accordingly, the gain and residual are updated by (20) and (23).

3) Step 3: In this step, the estimates of $(i+1)$ paths are cyclically refined by using the Newton refinement for R_c rounds. Note that the estimated parameters of the $(i+1)$ paths are denoted as $(\hat{d}_\ell, \hat{\theta}_\ell, \hat{\phi}_\ell), \ell = 0, ..., i$.

4) Step 4: In this step, the equivalent complex gains of all paths are re-estimated by the LS method as

$$[\hat{g}_0, ..., \hat{g}_i]^{\top} = \mathbf{U}^{\dagger}\mathbf{y}_{\mathrm{UR}}, \tag{26}$$

where $\mathbf{U} = \left[\grave{\mathbf{b}}(\hat{d}_0, \hat{\theta}_0, \hat{\phi}_0), ..., \grave{\mathbf{b}}(\hat{d}_i, \hat{\theta}_i, \hat{\phi}_i)\right]$. Given the estimated parameters $\{\hat{d}_l, \hat{\theta}_l, \hat{\phi}_l\}_{l=1}^{\hat{L}}$, and corresponding channel

gains $\hat{g}_l, l = 1, ..., \hat{L}$ of $\hat{L}$ paths, the channel between the UE and the RIS can be reconstructed as

$$\tilde{\mathbf{h}}_{\mathrm{UR}} = \sum_{l=1}^{\hat{L}} \hat{g}_l \mathbf{b}(\hat{d}_l, \hat{\theta}_l, \hat{\phi}_l). \tag{27}$$

C. RIS-BS Channel Reconstruction

As mentioned above, given the estimated LoS path of the RIS-BS channel $\widetilde{\mathbf{H}}_{\mathrm{RB}}^{\mathrm{LoS}}$ and $\tilde{\mathbf{h}}_{\mathrm{UR}}$, the NLoS components in the RIS-BS channel can be reconstructed through a joint uplink training and downlink training protocol. [4] Note that the BS can share the parameters estimated at the RIS through a backhaul link from the RIS to the BS. Then, the downlink transmission strategy including BS beamforming and RIS phase shifting strategy can be designed.

1) Estimation of parameters w.r.t. the BS: In this stage, the parameters w.r.t. the BS, i.e., $\{d_{\mathrm{B},s}, \theta_{\mathrm{B},s}, \phi_{\mathrm{B},s}\}_{s=1}^{S}$, can be estimated through the uplink pilots. When a portion of the RIS elements receive the uplink pilot of UE, the signal reflected by the other passive RIS elements is received by the BS as

$$\mathbf{y}_{\mathrm{B},t} = \sqrt{P_{\mathrm{U}}} \mathbf{W}_{\mathrm{B},t}^{\mathrm{UL}} \overline{\mathbf{H}}_{\mathrm{BR},t} \mathbf{\Theta}_t \overline{\mathbf{W}}_{\mathrm{R},t}^{\mathrm{UL}} \mathbf{h}_{\mathrm{UR}} x + \mathbf{n}_{\mathrm{B},t}, \tag{28}$$

where $\mathbf{W}_{\mathrm{B},t}^{\mathrm{UL}} \in \{0,1\}^{N_{\mathrm{B},t}^{\mathrm{UL}} \times N_{\mathrm{B}}}$ is the element selection matrix for BS receiving functionalities in time instance t, which has a single unity element in each row, $N_{\mathrm{B},t}^{\mathrm{UL}}$ is the number of BS elements for reception in the t-th instance, $\overline{\mathbf{W}}_{\mathrm{R},t}^{\mathrm{UL}} \in \{0,1\}^{\bar{N}_{\mathrm{R},t}^{\mathrm{UL}} \times N_{\mathrm{R}}}$ is the element selection matrix for RIS reflection, $\bar{N}_{\mathrm{R},t}^{\mathrm{UL}} = N_{\mathrm{R}} - N_{\mathrm{R},t}^{\mathrm{UL}}$ is the number of passive RIS elements for reflecting the uplink pilot, $\mathbf{\Theta}_t \in \mathbb{C}^{\bar{N}_{\mathrm{R},t}^{\mathrm{UL}} \times \bar{N}_{\mathrm{R},t}^{\mathrm{UL}}}$ is the diagonal phase shift matrix of RIS, whose elements can be set as random phase shifts, while $\overline{\mathbf{H}}_{\mathrm{BR},t} = \mathbf{H}_{\mathrm{BR}} \overline{\mathbf{W}}_{\mathrm{R},t}^{\mathrm{UL}\top} \in \mathbb{C}^{N_{\mathrm{B}} \times \bar{N}_{\mathrm{R},t}^{\mathrm{UL}}}$ is the channel between the reflective RIS elements and BS array elements.

Assuming that $N_{\mathrm{B}}^{\mathrm{UL}}$ BS elements are active in total, the received signal at the BS among $T_{\mathrm{B}}^{\mathrm{UL}} = \lceil N_{\mathrm{B}}^{\mathrm{UL}} / N_{\mathrm{RF,B}} \rceil$ time instances can be denoted as

$$\mathbf{y}_{\mathrm{B}} = \sqrt{P_{\mathrm{U}}} \mathbf{W}_{\mathrm{B}}^{\mathrm{UL}} \overline{\mathbf{H}}_{\mathrm{BR}} \mathbf{\Theta} \overline{\mathbf{W}}_{\mathrm{R}}^{\mathrm{UL}} \mathbf{h}_{\mathrm{UR}} x + \mathbf{n}_{\mathrm{B}}, \tag{29}$$

where $\mathbf{y}_{\mathrm{B}} = \left[\mathbf{y}_{\mathrm{B},1}^{\top}, ..., \mathbf{y}_{\mathrm{B},T_{\mathrm{B}}^{\mathrm{UL}}}^{\top}\right]^{\top}$ is the stacked received signals, $\mathbf{W}_{\mathrm{B}}^{\mathrm{UL}} = \left[\mathbf{W}_{\mathrm{B},1}^{\mathrm{UL}\top}, ..., \mathbf{W}_{\mathrm{B},T_{\mathrm{B}}^{\mathrm{UL}}}^{\mathrm{UL}\top}\right]^{\top}$ and $\mathbf{n}_{\mathrm{B}} = \left[\mathbf{n}_{\mathrm{B},1}^{\top}, ..., \mathbf{n}_{\mathrm{B},T_{\mathrm{B}}^{\mathrm{UL}}}^{\top}\right]^{\top}$ are the stacked element activation matrices and noise vectors of the BS, respectively. Note that $\mathbf{\Theta}_t$ and $\overline{\mathbf{W}}_{\mathrm{R},t}^{\mathrm{UL}}$ should stay constant among $T_{\mathrm{B}}^{\mathrm{UL}}$ time instances due to the BS hardware limitations. Henceforth, we simplify them as $\mathbf{\Theta}$ and $\overline{\mathbf{W}}_{\mathrm{R}}^{\mathrm{UL}}$, respectively. Based on (29), the partial parameters of RIS-BS channel w.r.t. the BS are extracted at the BS side. Assuming that all-one pilots are transmitted, (29) can be further written based on the RIS-BS channel model as

$$\mathbf{y}_{\mathrm{B}} = \sqrt{P_{\mathrm{U}}} \mathbf{W}_{\mathrm{B}}^{\mathrm{UL}} \sum_{s=1}^{S} g_s \mathbf{b}_{\mathrm{B}}(\Upsilon_{\mathrm{B},s}) \bar{\mathbf{b}}_{\mathrm{R}}^{\mathsf{H}}(\Upsilon_{\mathrm{R},s}) \mathbf{\Theta} \overline{\mathbf{W}}_{\mathrm{R}}^{\mathrm{UL}} \mathbf{h}_{\mathrm{UR}} + \mathbf{n}_{\mathrm{B}}, \tag{30}$$

[4] In this subsection, we assume that the influence of $\mathbf{H}_{\mathrm{RB}}^{\mathrm{LoS}}$ is eliminated from the received signal at the BS, which can be achieved via the accurately estimated $\tilde{\mathbf{H}}_{\mathrm{RB}}^{\mathrm{LoS}}$ and $\tilde{\mathbf{h}}_{\mathrm{UR}}$. For simplicity, we omit the superscript "NLoS" from $\mathbf{H}_{\mathrm{RB}}^{\mathrm{NLoS}}$ and $\mathbf{H}_{\mathrm{BR}}^{\mathrm{NLoS}}$ unless otherwise specified.

where $\bar{\mathbf{b}}_{\mathrm{R}}(\Upsilon_{\mathrm{R},s}) = \overline{\mathbf{W}}_{\mathrm{R}}^{\mathrm{UL}} \mathbf{b}_{\mathrm{R}}(\Upsilon_{\mathrm{R},s})$. Denoting $\beta_s = g_s \bar{\mathbf{b}}_{\mathrm{R}}^{\mathsf{H}}(\Upsilon_{\mathrm{R},s}) \mathbf{\Theta} \overline{\mathbf{W}}_{\mathrm{R}}^{\mathrm{UL}} \mathbf{h}_{\mathrm{UR}}$, the parameters of the RIS-BS channel w.r.t. the BS can be obtained by solving the following problem

$$\{\hat{d}_{\mathrm{B},s}, \hat{\theta}_{\mathrm{B},s}, \hat{\phi}_{\mathrm{B},s}\}_{s=1}^{\hat{S}} = \arg\min_{\{d,\theta,\phi\}} \left\| \mathbf{y}_{\mathrm{B}} - \sqrt{P} \mathbf{W}_{\mathrm{B}}^{\mathrm{UL}} \sum_{s=1}^{S} \beta_s \mathbf{b}_{\mathrm{B}}(d, \theta, \phi) \right\|^2. \tag{31}$$

The near-field NOMP algorithm described above can be applied in solving this problem with the codebook $\Omega_{\mathrm{B}}^{\mathrm{UL}}$, and we can get the estimated number of path $\hat{S}$ and parameters $\{\hat{d}_{\mathrm{B},s}, \hat{\theta}_{\mathrm{B},s}, \hat{\phi}_{\mathrm{B},s}\}_{s=1}^{\hat{S}}$. Considering the non-ideal sparsity of RIS-BS channel and limited number of NLoS paths [35], the max number of iterations can also be added to the stopping criterion.

2) Estimation of parameters w.r.t. the RIS: In the second stage, the remaining parameters in the RIS-BS channel are estimated at the RIS, and the BS sends downlink pilots to the RIS. In order to avoid the mismatch between parameters w.r.t. the RIS and parameters w.r.t. the BS, the downlink pilot is first beamformed based on the estimates of the RIS-BS channel, i.e., $\{\hat{d}_{\mathrm{B},s}, \hat{\theta}_{\mathrm{B},s}, \hat{\phi}_{\mathrm{B},s}\}_{s=1}^{\hat{S}}$. Then, the downlink pilots are designed as $\mathbf{X}_{\mathrm{B}} = \left[\mathbf{f}_1, ..., \mathbf{f}_{\hat{S}}\right]$, where $\mathbf{f}_s \in \mathbb{C}^{N_{\mathrm{B}} \times 1}$ is the equivalent beamforming vector of the s-th beam, satisfying $\mathbf{f}_s = \mathbf{F}_{\mathrm{RF}}^{(s)} \mathbf{f}_{\mathrm{BB}}^{(s)}$, where $\mathbf{F}_{\mathrm{RF}}^{(s)} \in \mathbb{C}^{N_{\mathrm{B}} \times N_{\mathrm{RF,B}}}$ and $\mathbf{f}_{\mathrm{BB}}^{(s)} \in \mathbb{C}^{N_{\mathrm{RF,B}} \times 1}$ are the analog BF matrix and digital combining vector of the s-th beam, respectively. Notably, the configuration of $\mathbf{F}_{\mathrm{RF}}^{(s)}$ and $\mathbf{f}_{\mathrm{BB}}^{(s)}$ can be realized by setting $\mathbf{F}_{\mathrm{RF}}^{(s)}$ to the phase of the equivalent BF vector $\mathbf{f}_s$ and $\mathbf{f}_{\mathrm{BB}}^{(s)} = \mathbf{1}_{N_{\mathrm{RF,B}}}$. The equivalent BF vector of the s-th beam is

$$\mathbf{f}_s = \sqrt{P_{\mathrm{B}}} \mathbf{b}(\hat{d}_{\mathrm{B},s}, \hat{\theta}_{\mathrm{B},s}, \hat{\phi}_{\mathrm{B},s}) / \|\mathbf{b}(\hat{d}_{\mathrm{B},s}, \hat{\theta}_{\mathrm{B},s}, \hat{\phi}_{\mathrm{B},s})\|. \tag{32}$$

When the BS transmits the s-th beam, the downlink signal received by the RIS is

$$\mathbf{y}_{\mathrm{RB},s} = \mathbf{W}_{\mathrm{R}}^{\mathrm{DL}} \mathbf{H}_{\mathrm{RB}} \mathbf{f}_s + \mathbf{n}_{\mathrm{R},s}, \tag{33}$$

where $\mathbf{W}_{\mathrm{R}}^{\mathrm{DL}} = \left[\mathbf{W}_{\mathrm{R},1}^{\mathrm{DL}\top}, ..., \mathbf{W}_{\mathrm{R},T_{\mathrm{D}}}^{\mathrm{DL}\top}\right]^{\top} \in \{0,1\}^{N_{\mathrm{R}}^{\mathrm{DL}} \times N_{\mathrm{R}}}$ is the stacked downlink selection matrix for RIS, where $\mathbf{W}_{\mathrm{R},t}^{\mathrm{DL}}$ is the element selection matrix at the t-th time instance, $N_{\mathrm{R}}^{\mathrm{DL}}$ is the number of active RIS elements in downlink training, while $T_{\mathrm{D}} = \lceil \frac{N_{\mathrm{R}}^{\mathrm{DL}}}{N_{\mathrm{RF,R}}} \rceil$. Stacking the $\hat{S}$ beams, we obtain

$$\mathbf{Y}_{\mathrm{RB}} = \mathbf{W}_{\mathrm{R}}^{\mathrm{DL}} \mathbf{H}_{\mathrm{RB}} \mathbf{X}_{\mathrm{B}} + \mathbf{N}_{\mathrm{R}}, \tag{34}$$

where $\mathbf{Y}_{\mathrm{RB}} \in \mathbb{C}^{N_{\mathrm{R}}^{\mathrm{DL}} \times \hat{S}}$ satisfies $\mathbf{Y}_{\mathrm{RB}} = \left[\mathbf{y}_{\mathrm{RB},1}, ..., \mathbf{y}_{\mathrm{RB},\hat{S}}\right]$, and $\mathbf{N}_{\mathrm{R}}$ is the AWGN, satisfying $\mathrm{vec}(\mathbf{N}_{\mathrm{R}}) \sim \mathcal{CN}(\mathbf{0}, \sigma^2 \mathbf{I})$.

Specifically, the received s-th beam at the active elements of the RIS is

$$\mathbf{y}_{\mathrm{RB},s} = \mathbf{W}_{\mathrm{R}}^{\mathrm{DL}} \sum_{s=1}^{S} g_s \mathbf{b}_{\mathrm{R}}(\Upsilon_{\mathrm{R},s}) \mathbf{b}_{\mathrm{B}}^{\mathsf{H}}(\Upsilon_{\mathrm{B},s}) \mathbf{f}_s + \mathbf{n}_{\mathrm{R},s}. \tag{35}$$

Defining $\kappa_s \triangleq g_s \mathbf{b}_{\mathrm{B}}^{\mathsf{H}}(\Upsilon_{\mathrm{B},s}) \mathbf{f}_s$, (35) can be represented as

$$\mathbf{y}_{\mathrm{RB},s} = \mathbf{W}_{\mathrm{R}}^{\mathrm{DL}} \kappa_s \mathbf{b}_{\mathrm{R}}(\Upsilon_{\mathrm{R},s}) + \breve{\mathbf{n}}_{\mathrm{RB},s}, \tag{36}$$

Algorithm 1 Proposed Channel Reconstruction Scheme.

Input: Received signals $\mathbf{y}_{\mathrm{UR}}$, $\mathbf{y}_{\mathrm{B}}$, and $\mathbf{Y}_{\mathrm{RB}}$, location grids $\Omega_{\mathrm{R}}^{\mathrm{UL}}$, $\Omega_{\mathrm{B}}^{\mathrm{UL}}$, and $\Omega_{\mathrm{R}}^{\mathrm{DL}}$, elements selection matrices $\mathbf{W}_{\mathrm{R}}^{\mathrm{UL}}$, $\mathbf{W}_{\mathrm{B}}^{\mathrm{UL}}$, and $\mathbf{W}_{\mathrm{R}}^{\mathrm{DL}}$, and estimated $\widetilde{\mathbf{H}}_{\mathrm{RB}}^{\mathrm{LoS}}$.
Output: $\tilde{\mathbf{h}}_{\mathrm{UR}}$ and $\widetilde{\mathbf{H}}_{\mathrm{RB}}$.
Uplink training procedure:
Execute the near-field NOMP algorithm with $\mathbf{y}_{\mathrm{UR}}$, $\mathbf{W}_{\mathrm{R}}^{\mathrm{UL}}$ and $\Omega_{\mathrm{R}}^{\mathrm{UL}}$ to obtain $\tilde{\mathbf{h}}_{\mathrm{UR}}$;
Execute the near-field NOMP algorithm with $\mathbf{y}_{\mathrm{B}}$, $\mathbf{W}_{\mathrm{B}}^{\mathrm{UL}}$ and $\Omega_{\mathrm{B}}^{\mathrm{UL}}$ to obtain the estimates of the parameters w.r.t. the BS $\{\hat{d}_{\mathrm{B},s}, \hat{\theta}_{\mathrm{B},s}, \hat{\phi}_{\mathrm{B},s}\}_{s=1}^{\hat{S}}$;
Downlink training procedure:
Execute downlink training through (32) and obtain $\mathbf{X}_{\mathrm{B}}$;
for $s \leftarrow 1$ **to** $\hat{S}$ **do do**
Execute the matching step and Newton refinement step of near-field NOMP algorithm with input $[\mathbf{Y}_{\mathrm{RB}}]_{:,s}$, $\mathbf{W}_{\mathrm{R}}^{\mathrm{DL}}$, and $\Omega_{\mathrm{R}}^{\mathrm{DL}}$ to obtain $\{\hat{d}_{\mathrm{R},s}, \hat{\theta}_{\mathrm{R},s}, \hat{\phi}_{\mathrm{R},s}\}_{s=1}^{\hat{S}}$;
end for
Calculate the gains of the propagation paths based on (38).
Reconstruct the NLoS paths $\widetilde{\mathbf{H}}_{\mathrm{RB}}^{\mathrm{NLoS}}$ based on (39);
Reconstruct the RIS-BS channel $\widetilde{\mathbf{H}}_{\mathrm{RB}}$ based on (40).
return $\tilde{\mathbf{h}}_{\mathrm{UR}}$ and $\widetilde{\mathbf{H}}_{\mathrm{RB}}$.

where $\breve{\mathbf{n}}_{\mathrm{RB},s} = \mathbf{W}_{\mathrm{R}}^{\mathrm{DL}} \sum_{i \neq s} g_i \mathbf{b}_{\mathrm{R}}(\Upsilon_{\mathrm{R},i}) \mathbf{b}_{\mathrm{B}}^{\mathsf{H}}(\Upsilon_{\mathrm{B},i}) \mathbf{f}_i + \mathbf{n}_{\mathrm{R},s}$ is the equivalent noise term. The parameters of the RIS-BS channel paired with $\{\hat{d}_{\mathrm{B},s}, \hat{\theta}_{\mathrm{B},s}, \hat{\phi}_{\mathrm{B},s}\}$ are obtained by solving the following problem

$$\begin{aligned} &\{\hat{d}_{\mathrm{R},s}, \hat{\theta}_{\mathrm{R},s}, \hat{\phi}_{\mathrm{R},s}\} \\ &\quad = \arg\min_{d,\theta,\phi} \left\| \mathbf{y}_{\mathrm{RB},s} - \mathbf{W}_{\mathrm{R}}^{\mathrm{DL}} \kappa_s \mathbf{b}_{\mathrm{R}}(d,\theta,\phi) \right\|^2. \end{aligned} \tag{37}$$

We just use the initial matching with codebook $\Omega_{\mathrm{R}}^{\mathrm{DL}}$ and Newton refinement step in the near-field NOMP Algorithm to solve the problem above. After executing the procedure for $s = 1, ..., \hat{S}$ cyclically, the gains of the RIS-BS channel, $\{\hat{g}_s\}_{s=1}^{\hat{S}}$, are calculated by the LS as

$$[\hat{g}_1, ..., \hat{g}_{\hat{S}}]^{\top} = \mathbf{\Lambda}^{\dagger} \operatorname{vec}(\mathbf{Y}_{\mathrm{RB}}), \tag{38}$$

where $\mathbf{\Lambda} = [\operatorname{vec}(\mathbf{B}_1 \mathbf{X}_{\mathrm{B}}), ..., \operatorname{vec}(\mathbf{B}_{\hat{S}} \mathbf{X}_{\mathrm{B}})]$, and $\mathbf{B}_s = \mathbf{W}_{\mathrm{R}}^{\mathrm{DL}} \mathbf{b}_{\mathrm{R}}(\hat{\Upsilon}_{\mathrm{R},s}) \mathbf{b}_{\mathrm{B}}^{\mathsf{H}}(\hat{\Upsilon}_{\mathrm{B},s})$.

Afterwards, the NLoS paths of the channel between RIS and BS can be reconstructed as

$$\widetilde{\mathbf{H}}_{\mathrm{RB}}^{\mathrm{NLoS}} = \sum_{s=1}^{\hat{S}} \hat{g}_s \mathbf{b}_{\mathrm{R}}(\hat{d}_{\mathrm{R},s}, \hat{\theta}_{\mathrm{R},s}, \hat{\phi}_{\mathrm{R},s}) \mathbf{b}_{\mathrm{B}}^{\mathsf{H}}(\hat{d}_{\mathrm{B},s}, \hat{\theta}_{\mathrm{B},s}, \hat{\phi}_{\mathrm{B},s}). \tag{39}$$

With the estimated $\widetilde{\mathbf{H}}_{\mathrm{RB}}^{\mathrm{LoS}}$, the estimated RIS-BS channel is

$$\widetilde{\mathbf{H}}_{\mathrm{RB}} = \widetilde{\mathbf{H}}_{\mathrm{RB}}^{\mathrm{LoS}} + \widetilde{\mathbf{H}}_{\mathrm{RB}}^{\mathrm{NLoS}}. \tag{40}$$

The framework of the proposed channel reconstruction scheme is summarized in Algorithm 1.

TABLE II
PILOT OVERHEAD COMPARISION OF DIFFERENT CHANNEL ESTIMATION SCHEMES

RIS type	Channel estimation scheme	Pilot overhead
Passive RIS [14]	Traditional	256
Passive RIS [16]	ANM	98
Hybrid RIS [20]	ANM	42
Hybrid RIS [21]	ANM	160
Hybrid RIS [22]	CS-based	32
Sensing RIS	**Proposed**	**11**

D. Pilot Overhead Analysis

The training overhead of the proposed channel reconstruction scheme is

$$T_{\mathrm{p}} = T_{\mathrm{U}} + T_{\mathrm{B}}^{\mathrm{UL}} - 1 + \hat{S} T_{\mathrm{D}}.^{5} \tag{41}$$

It can be observed that the training overhead is determined by the number of active RIS elements and BS elements. To further demonstrate the superiority of the proposed channel reconstruction scheme and sensing RIS structure in reducing the training overhead, we make the following comparison. We first consider the non-structured channel based on passive RISs, for which the training overhead is N_{R} for a single-antenna UE [14]. As for the structured channel, [16] proposed an ANM-based algorithm for passive RISs and the training overhead is $N_{\text{passive1}} + N_{\text{passive2}} L$, where N_{passive1} and N_{passive2} are the numbers of training beams in two stages, respectively. For hybrid RIS structures, an ANM-based scheme was considered in [20] and the training overhead is $\lceil \frac{N_{\mathrm{R}}^{\mathrm{UL}}}{N_{\mathrm{RF,R}}} \rceil + N_{\text{hybrid1}} \lceil \frac{N_{\mathrm{B}}^{\mathrm{DL}}}{N_{\mathrm{RF,R}}} \rceil$, where N_{hybrid1} is the number of downlink training beams. Another ANM-based scheme was proposed in [21] and its training overhead is $N_{\text{hybrid2}} \lceil \frac{N_{\mathrm{R}}^{\mathrm{UL}}}{N_{\mathrm{RF,R}}} \rceil \lceil \frac{N_{\mathrm{B}}^{\mathrm{UL}}}{N_{\mathrm{RF,B}}} \rceil$, which can be simplified as N_{hybrid2} since fully digital structures are considered in both the RIS and BS, while N_{hybrid2} is the equivalent length of training sequence defined in [21]. CS based algorithms were adopted in [22] and the resulting training overhead is N_{hybrid3}, where N_{hybrid3} is the number of combinations for the analog BF structure in RIS.

To be more specific, we consider the same system configuration as: $N_{\mathrm{B}} = N_{\mathrm{R}} = 256$, $N_{\mathrm{RF,B}} = N_{\mathrm{RF,R}} = 32$, $N_{\mathrm{R}}^{\mathrm{UL}} = N_{\mathrm{B}}^{\mathrm{UL}} = N_{\mathrm{R}}^{\mathrm{DL}} = 64$, $\hat{S} = S = 4$. Notably, the parameters related to the length of training sequence defined by the authors in [14], [16], [20]–[22] are set the same with the original papers, i.e. $N_{\text{passive1}} = N_{\text{passive2}} = 14$, $N_{\text{hybrid1}} = 20$, $N_{\text{hybrid2}} = 40$ and $N_{\text{hybrid3}} = 32$. Then, we calculate the training overhead of different algorithms, as listed in Table II. It is clearly seen that the proposed channel reconstruction scheme entails the minimal training overhead, since it avails of this flexible sensing RIS structure and the efficient training protocol.

E. Computational Complexity Analysis

In this section, we analyze the computational complexity of the proposed channel reconstruction scheme. In the first

[5]The -1 means that the training of $\mathbf{h}_{\mathrm{UR}}$ and $\{\Upsilon_{\mathrm{B},s}\}_{s=1}^{S}$ can share one time instance. Note that if less elements are required for a slightly changing channel, the two aforementioned steps are executed simultaneously.

stage, the computational complexity of the UE-RIS channel mainly depends on the NOMP algorithm. The complexity of new path detection, single refinement, cyclic refinement and gains update is $\mathcal{O}\left(|\Omega_{\mathrm{R}}^{\mathrm{UL}}|\hat{L}N_{\mathrm{R}}^{\mathrm{UL}}N_{\mathrm{R}}\right)$, $\mathcal{O}\left(R_s\hat{L}N_{\mathrm{R}}^{\mathrm{UL}}\right)$, $\mathcal{O}\left(R_cR_s\hat{L}^2N_{\mathrm{R}}^{\mathrm{UL}}\right)$, and $\mathcal{O}\left(\hat{L}^3N_{\mathrm{R}}^{\mathrm{UL}}\right)$, respectively. Similarly, the computational complexity of the parameters of RIS-BS channel w.r.t. the BS is $\mathcal{O}\left(|\Omega_{\mathrm{B}}^{\mathrm{UL}}|\hat{S}N_{\mathrm{B}}^{\mathrm{UL}}N_{\mathrm{B}}\right) + \mathcal{O}\left(R_s\hat{S}N_{\mathrm{B}}^{\mathrm{UL}}\right) + \mathcal{O}\left(R_cR_s\hat{S}^2N_{\mathrm{B}}^{\mathrm{UL}}\right)$, where each term corresponds to a different step in the NOMP algorithm. In the second stage, the computational complexity is $\mathcal{O}\left(|\Omega_{\mathrm{R}}^{\mathrm{UL}}|\hat{S}N_{\mathrm{R}}^{\mathrm{DL}}N_{\mathrm{R}}\right) + \mathcal{O}\left(R_s\hat{S}N_{\mathrm{R}}^{\mathrm{DL}}\right) + \mathcal{O}\left(\hat{S}^3N_{\mathrm{R}}^{\mathrm{DL}}\right)$. We can observe that the computational complexity increases with $|\Omega_{\mathrm{R}}^{\mathrm{UL}}|$, $|\Omega_{\mathrm{B}}^{\mathrm{UL}}|$ and $|\Omega_{\mathrm{R}}^{\mathrm{DL}}|$, which may be further reduced through searching the combination of grids in the distance and angular domains. However, it can be concluded that compared with the method proposed in [24], we solve the RIS-BS channel reconstruction problem through two steps, which reduces the computational complexity effectively at the cost of moderate training overhead.

IV. RIS Pattern Configuration

To decide which RIS elements the signals impinge on should be selected for signal processing, an RIS pattern is introduced by considering the topology of the active RIS elements, determined by the element selection matrices $\mathbf{W}_{\mathrm{R}}^{\mathrm{UL}}$ and $\mathbf{W}_{\mathrm{R}}^{\mathrm{DL}}$. Based on the high flexibility of this sensing RIS structure, both the number of active RIS elements and the RIS pattern can vary to achieve different estimation accuracy. In this section, we aim to select a superior RIS pattern configuration and then we investigate the influence of RIS pattern configuration on the proposed channel reconstruction scheme from a theoretical perspective. Specifically, we compare the radiation pattern and parameter estimation accuracy of different RIS pattern configurations, and prove the superiority of random pattern based on the two aspects above. For notational convenience, the element selection matrix and the set of active elements are denoted as $\mathbf{W}_{\mathrm{R}}^{\mathrm{act}} \in \mathbb{C}^{N_{\mathrm{R}}^{\mathrm{act}}\times N_{\mathrm{R}}}$ and $\mathcal{N}_{\mathrm{R}}^{\mathrm{act}}$, respectively, where $N_{\mathrm{R}}^{\mathrm{act}}$ is the number of active elements.

A. Pattern Types

In this section, we consider the following pattern types. *Full Pattern* means all N_{R} RIS elements are active, which is expected to achieve the performance benchmark. *Random Pattern* randomly selects $N_{\mathrm{R}}^{\mathrm{act}}$ elements from the full pattern, as shown in Fig. 4(a). Existing research indicates that the random pattern is an efficient solution (see [34], [36]). A *Sparse Array* is a kind of designed patterns which have been widely researched due to their advantages in reducing mutual coupling [37], [38]. However, the pattern of sparse arrays is always fixed and the numbers of elements in sparse arrays always follow certain rules. *Successive Pattern* refers to $N_{\mathrm{R}}^{\mathrm{act}}$ elements forming a half-wavelength spaced UPA. For a sparse array, as shown in Fig. 4(b), we select the half open box array (HOBA) type due to its superior properties, in which

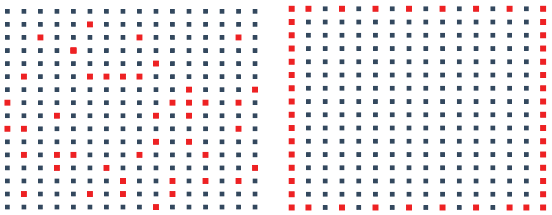

(a) Random pattern (b) HOBA pattern

Fig. 4. Illustration of the random pattern and the HOBA pattern with the same number of active elements (denoted by red squares).

46 elements are active, and the size of the successive pattern is 8×6, with a similar number of active elements to the HOBA pattern.

B. Radiation Pattern

Since the first step of the near-field NOMP algorithm is matching with the dictionary, we evaluate the radiation pattern. This metric can intuitively show the resolution and directivity of each pattern type. For a fixed $(\ddot{d},\ddot{\theta},\ddot{\phi})$,

$$G(d_i,\theta_i,\phi_i)=\frac{|(\mathbf{W}_{\mathrm{R}}^{\mathrm{act}}\mathbf{b}(d_i,\theta_i,\phi_i))^{\mathsf{H}}\mathbf{W}_{\mathrm{R}}^{\mathrm{act}}\mathbf{b}(\ddot{d},\ddot{\theta},\ddot{\phi})|}{\|\mathbf{W}_{\mathrm{R}}^{\mathrm{act}}\mathbf{b}(d_i,\theta_i,\phi_i)\|^2}, \quad (42)$$

is the projected power on (d_i,θ_i,ϕ_i). Drawing $G(d_i,\theta_i,\phi_i)$ on all $(d_i,\theta_i,\phi_i)\in\Omega$, we can obtain the radiation pattern, where Ω is the grid dictionary. Note that the influence of different RIS patterns is reflected through $\mathbf{W}_{\mathrm{R}}^{\mathrm{act}}$. In the following, we illustrate the radiation pattern from two aspects: radiation pattern w.r.t. distance and radiation pattern w.r.t. angles.

1) Radiation Pattern w.r.t. distance: Firstly, we compare the radiation pattern in the distance domain when the angles of each sampling point in Ω is known a priori. Thus, $G(d_i,\theta_i,\phi_i)$ is simplified as $G(d_i)$. The distance term D_n in (3) can be approximated through the Taylor series, where l is omitted in the superscript and subscript, such that

$$\begin{aligned}D_n \approx\ & d-(y_{n_h}\sin\theta\sin\phi+z_{n_v}\cos\theta)\\ &+\frac{1}{2d}(y_{n_h}^2+z_{n_v}^2-(y_{n_h}\sin\theta\sin\phi+z_{n_v}\cos\theta)^2).\end{aligned} \quad (43)$$

For a given $\ddot{d}$, $G(d_i)$ can be calculated approximately as (44), shown at the bottom of next page. Then, the following proposition can be derived.

Proposition 1: For a predefined position $\ddot{d}$, the expectation of $G(d_i)$ w.r.t. the random $\mathbf{W}_{\mathrm{R}}^{\mathrm{act}}$ satisfies $\mathbb{E}_{\mathbf{W}_{\mathrm{R}}^{\mathrm{act}}}\{G(d_i)\}\approx G_{\mathrm{full}}(d_i)$, where $G_{\mathrm{full}}(d_i)$ is the radiation pattern derived by the full pattern.

Proof: See Appendix A. ■

We set $(\ddot{d},\ddot{\theta},\ddot{\phi})$ as $(30\lambda,\frac{\pi}{2},0)$ and $(80\lambda,\frac{\pi}{2},0)$, respectively. Figure 5(a) presents the radiation pattern w.r.t. the distance of different RIS patterns. Note that the number of random elements is equal to the number of elements in the HOBA pattern, i.e., 46 elements. It can be observed that all RIS patterns reach their maximum value at the predefined location, while the Monte-Carlo results of a random pattern reach close radiation performance to the full pattern at different UE positions, which verifies Proposition 1. Moreover, by

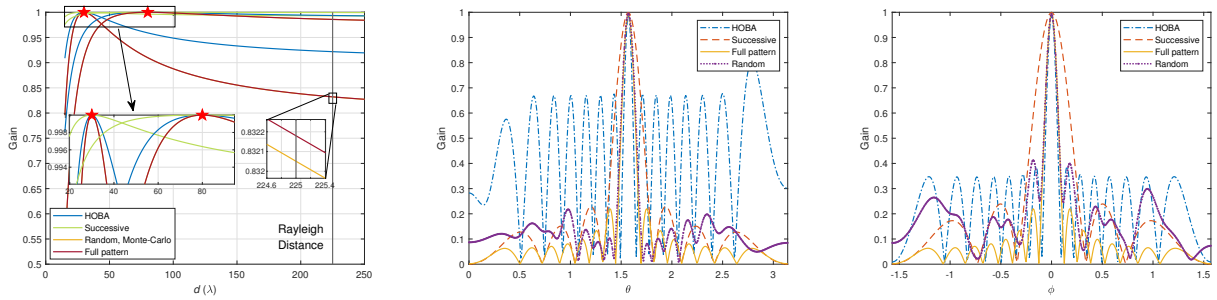

(a) Radiation pattern w.r.t. d (b) Radiation pattern w.r.t. θ (c) Radiation pattern w.r.t. ϕ

Fig. 5. Illustration of the radiation pattern w.r.t d, θ and ϕ, respectively.

comparing the performance of sparse array, successive array and random pattern, the random pattern is also proven to be an effective RIS pattern. However, when increasing the distance, the performance gaps between different RIS patterns tend to be narrow. The phenomenon can be attributed to (43) in which the distance term is in the denominator when omitting the same term d for all D_n. Hence, the influence of distance is reduced for a higher distance.

2) Radiation Pattern w.r.t. angles: Next, we compare the radiation pattern in the angular domain. We set $(\ddot{d}, \ddot{\theta}, \ddot{\phi}) = (50\lambda, \frac{\pi}{2}, 0)$ and the distance is assumed to be perfectly known in the dictionary Ω. As shown in Fig. 5, we compare the radiation pattern in the angular domain under different array patterns. In accordance with [39], looking at the random array pattern, the mainlobe width is related to the effective array aperture. Moreover, the level of sidelobes is related to the number of random elements. It can be observed from Fig. 5(b) and Fig. 5(c) that the mainlobe of the successive pattern is wider than that of other array patterns, because the successive layout reduces the effective array aperture and results in a wider mainlobe. The random pattern generates a similar mainlobe with the full pattern since the randomly distributed elements span across the full array. The mainlobe generated by a sparse array w.r.t. ϕ is similar with full pattern, while the mainlobe w.r.t. θ is narrow but with high level of sidelobes. According to the layout of HOBA, the inter-element spacing is $\frac{\lambda}{2}$ in the vertical direction but larger than λ in the horizontal direction. The widened antenna space leads to narrower mainlobe but higher sidelobe or even grating lobes. Based on the analysis above, it can be concluded that the random pattern is an effective array pattern.

3) Parameter Estimation Accuracy: Next, we evaluate the parameter estimation accuracy by deriving the Cramér-Rao lower bound (CRLB), which represents the lower-bound variance of the unbiased estimation. We first define $\boldsymbol{\varpi}_l = [d_l, \theta_l, \phi_l]$ and $\boldsymbol{\varpi} = [\boldsymbol{\varpi}_1, ..., \boldsymbol{\varpi}_L]$. Based on the channel model in (15), the $3L \times 3L$ Fisher information matrix (FIM) can be defined as [40]

$$\mathbf{F}(\boldsymbol{\varpi}) = \begin{bmatrix} \mathbf{F}_{11}(\boldsymbol{\varpi}) & \dots & \mathbf{F}_{1L}(\boldsymbol{\varpi}) \\ \vdots & \ddots & \vdots \\ \mathbf{F}_{L1}(\boldsymbol{\varpi}) & \dots & \mathbf{F}_{LL}(\boldsymbol{\varpi}) \end{bmatrix}, \tag{45}$$

where the 3×3 matrices $\mathbf{F}_{ll}(\boldsymbol{\varpi}), l = 1, ..., L$ are defined as

$$\mathbf{F}_{ll}(\boldsymbol{\varpi}) = \frac{2P_{\mathrm{U}}}{\sigma_n^2} \Re \left\{ \left(\frac{\partial \grave{\mathbf{b}}(\boldsymbol{\varpi})}{\partial \boldsymbol{\varpi}_l} \right)^{\mathsf{H}} \left(\frac{\partial \grave{\mathbf{b}}(\boldsymbol{\varpi})}{\partial \boldsymbol{\varpi}_l} \right) \right\}, \tag{46}$$

where $\grave{\mathbf{b}}(\boldsymbol{\varpi}) = \sum_{l=1}^{L} g_l \grave{\mathbf{b}}(d_l, \theta_l, \phi_l)$, while the matrices $\mathbf{F}_{ll'}(\boldsymbol{\varpi})$ are defined as $\mathbf{F}_{ll'}(\boldsymbol{\varpi}) = \mathbf{0}, l, l' = 1, ..., L, l \neq l'$ due to the uncorrelated $g_l, l = 1, ..., L$. Therefore, the CRLB of distance and angles is written as

$$\mathrm{CRLB}_d = \textstyle\sum_{l=1}^{L} \left[\mathbf{F}^{-1}(\boldsymbol{\varpi})\right]_{3l-2,3l-2}, \tag{47a}$$

$$\mathrm{CRLB}_\theta = \textstyle\sum_{l=1}^{L} \left[\mathbf{F}^{-1}(\boldsymbol{\varpi})\right]_{3l-1,3l-1}, \tag{47b}$$

$$\mathrm{CRLB}_\phi = \textstyle\sum_{l=1}^{L} \left[\mathbf{F}^{-1}(\boldsymbol{\varpi})\right]_{3l,3l}. \tag{47c}$$

To exploit the relationship between the number of active elements and full pattern, we derive the following proposition.

Proposition 2: The expectation of CRLB w.r.t. the random $\mathbf{W}_{\mathrm{R}}^{\mathrm{act}}$, for a fixed target position (d, θ, ϕ), derived by random active elements, satisfies

$$\mathbb{E}_{\mathbf{W}_{\mathrm{R}}^{\mathrm{act}}}\{\mathrm{CRLB}_x\} \approx \frac{N_{\mathrm{R}}}{N_{\mathrm{R}}^{\mathrm{act}}} \mathrm{CRLB}_{x,\mathrm{full}}, x \in \{d, \theta, \phi\}, \tag{48}$$

where $\mathrm{CRLB}_{x,\mathrm{full}}$ is the CRLB of parameter x derived by the full pattern.

Proof: See Appendix B. ∎

Proposition 2 unveils that the estimation accuracy of the random pattern is proportional to the number of active RIS elements. Figure 6 compares the CRLB of parameters against the number of random elements with other RIS patterns. The number of multipaths is set as $L = 6$ and the transmit signal -to-noise ratio (SNR) is set as $P_{\mathrm{U}}/\sigma_n^2 = 5$ dB. It can be observed that if the positions of scatterers are fixed, the scaled

$$G(d_i) \approx \frac{1}{N_{\mathrm{R}}^{\mathrm{act}}} \left| \sum_{n \in \mathcal{N}_{\mathrm{R}}^{\mathrm{act}}} \exp\left(\jmath\pi \left(\frac{1}{d_i} - \frac{1}{\ddot{d}} \right) \left(y_{n_h}^2 + z_{n_v}^2 - (y_{n_h} \sin\theta \sin\phi + z_{n_v} \cos\theta)^2 \right) \right) \right| \tag{44}$$

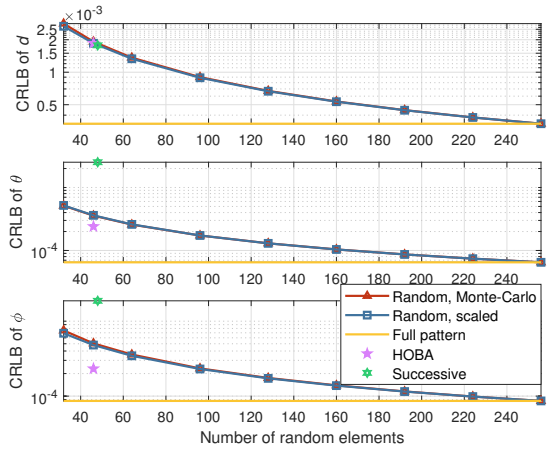

Fig. 6. CRLB versus the number of active RIS elements.

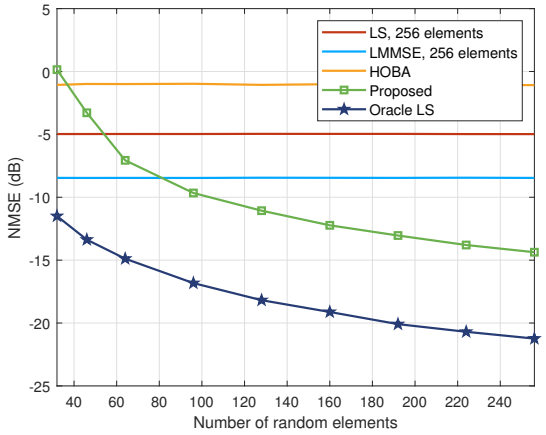

Fig. 7. The NMSE of UE-RIS channel versus the number of random elements.

CRLB of the random pattern is close to the full pattern, which validates Proposition 2. Although the CRLB derived for a sparse array is lower than the random pattern, the sparse arrays face the limitation of fixed patterns. Note that the CRLB is the theoretically lower bound that is independent of the estimation algorithm. The real estimation accuracy varies by using different estimation algorithms, which will be further analyzed in Section V-A.

In accordance with the analysis above, the effectiveness of random pattern can be summarized as: 1) high flexibility, 2) similar radiation pattern with full pattern, and 3) scaled estimation accuracy of full pattern. Therefore, we employ the random pattern configuration in the proposed channel reconstruction scheme.

V. Numerical Results

In this section, we evaluate the performance of the proposed channel reconstruction scheme with the sensing RIS structure. In this RIS-assisted system, we consider the sub-6GHz frequency band and $f_c = 3.0$ GHz.[6] For the UPA at the BS, we set $N_{\mathrm{B}h} = N_{\mathrm{B}v} = 16$ and $N_{\mathrm{B}} = 256$. For the RIS, we consider the same dimension with the UPA at the BS, i.e. $N_{\mathrm{R}h} = N_{\mathrm{R}v} = 16$ and $N_{\mathrm{R}} = 256$. The number of RF chains for the BS and the RIS are $N_{\mathrm{RF,B}} = N_{\mathrm{RF,R}} = 32$, respectively. The position of scatterers in the UE-RIS channel satisfies: $d_l \sim \mathcal{U}[20\lambda, 200\lambda]$, $\theta_l \sim \mathcal{U}[\frac{\pi}{3}, \frac{2\pi}{3}]$ and $\phi_l \sim \mathcal{U}[-\frac{\pi}{3}, \frac{\pi}{3}]$, while the scatterers in the RIS-BS channel are distributed as: $d_{X,s} \sim \mathcal{U}[20\lambda, 100\lambda]$, $\theta_{X,s} \sim \mathcal{U}[\frac{\pi}{3}, \frac{2\pi}{3}]$ and $\phi_{X,s} \sim \mathcal{U}[-\frac{\pi}{3}, \frac{\pi}{3}]$, $X \in \{\mathrm{R}, \mathrm{B}\}$, where the distances are all in accordance with the conditions of Fresnel region [29]. The number of multipaths in UE-RIS channel and RIS-BS channel is set as $L = 6$ and $S = 4$, respectively, and the channel gains are modeled as $g_l \sim \mathcal{CN}(0,1), l = 1, ..., L$ and $g_s \sim \mathcal{CN}(0,1), s = 1, ..., S$, respectively. For the NOMP algorithm, the sizes of the dictionary $\Omega_{\mathrm{R}}^{\mathrm{UL}}$, $\Omega_{\mathrm{B}}^{\mathrm{UL}}$ and $\Omega_{\mathrm{R}}^{\mathrm{DL}}$ are all $10 \times 32 \times 32$ ($N_d \times N_\theta \times N_\phi$) for the UE-RIS channel and RIS-BS channel. For the geometric relationship between the RIS and BS, we set $d_{\mathrm{RB}} = 30\lambda$ and $\vartheta_{\mathrm{RB}} = \frac{\pi}{4}$. The coherence time is $T_{\mathrm{c}} = 600$.

[6]From the over-the-air test results in [41], it can be inferred that the channel power is concentrated on few reconstructed paths even at the sub-6GHz frequency band, especially under scenarios such as indoor scenarios or outdoor scenarios at close range. Therefore, it is rational to model the channel through the finite-dimensional channel model.

A. UE-RIS Channel Reconstruction

The accuracy of the UE-RIS channel reconstruction is evaluated by the normalized mean square error (NMSE)

$$\mathrm{NMSE}_{\mathrm{UR}} = \frac{\|\mathbf{h}_{\mathrm{UR}} - \tilde{\mathbf{h}}_{\mathrm{UR}}\|^2}{\|\mathbf{h}_{\mathrm{UR}}\|^2}, \tag{49}$$

and the transmit SNR is defined as $P_{\mathrm{U}}/\sigma_n^2$. Figure 7 evaluates the NMSE performance of the UE-RIS channel reconstruction scheme w.r.t. the number of random elements when the SNR is 5 dB. Traditional methods, including LS and LMMSE, are compared as benchmarks whilst the oracle LS, in which the parameters $\{d_l, \theta_l, \phi_l\}_{l=1}^L$ are perfectly known, is the lower bound. As can be observed from Fig. 7, the extrapolated channel through only a quarter of random elements reaches a comparable NMSE with traditional schemes, which means that the training overhead is also a quarter of the traditional methods. As expected, a more accurate channel can be reconstructed by increasing the number of random RIS elements, which means that the number of active RIS elements can be adjusted according to the expected channel estimation accuracy in different conditions. Moreover, the error of the reconstructed channel, derived by the random pattern, is still lower than that of the HOBA pattern, which is caused by the high sidelobes of the latter.

Figure 8 evaluates the NMSE performance of the UE-RIS channel reconstruction scheme against the transmit SNR, when the numbers of active RIS $N_{\mathrm{R}}^{\mathrm{UL}}$ are set as 64 and 128, denoted as setup 1 and setup 2, respectively. The proposed UE-RIS channel reconstruction scheme is compared with the hierarchical matching method in [13], and the Orthogonal Matching Pursuit (OMP) with a DFT codebook [42], while the oracle LS is also considered as a lower bound. The proposed method can extract more accurate parameters compared with the traditional hierarchical matching methods. As expected,

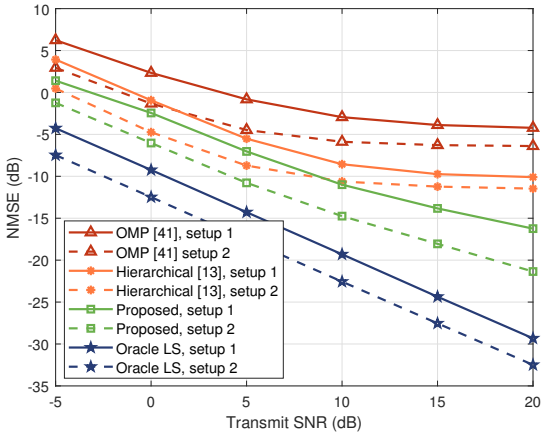

Fig. 8. The NMSE of UE-RIS channel versus the transmit SNR.

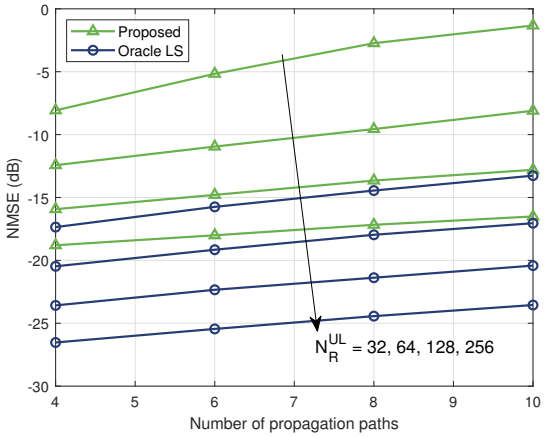

Fig. 9. The NMSE of UE-RIS channel versus the number of propagation paths.

increasing the active RIS elements is an effective way to improve the NMSE performance by comparing the solid curves with the dotted curves. It can also be seen that the performance of the proposed UE-RIS channel reconstruction scheme is close to that of the oracle LS, which also validates the accuracy of parameter estimation in the proposed scheme.

Figure 9 illustrates the NMSE performance of UE-RIS channel reconstruction against the number of propagation paths for different numbers of active RIS elements when the SNR is 10 dB. Furthermore, the oracle LS method for different numbers of active RIS elements is also acting as a lower bound. It can be verified that the proposed scheme achieves accurate UE-RIS channel estimation when different numbers of propagation paths are considered. Moreover, when the number of active RIS elements is small, the gap between the proposed method and lower bounds is unstable. However, when more elements are active, the performance gap between the proposed scheme and the oracle LS is stable, which means that the former shows robustness to the number of propagation paths. Thus, the proposed scheme is verified to be an effective method for the sub-6GHz frequency band.

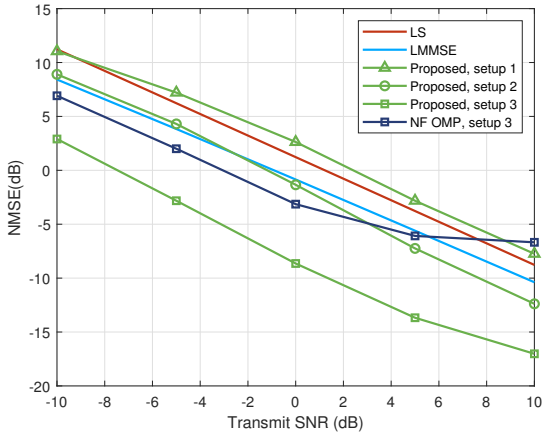

Fig. 10. The NMSE of RIS-BS channel versus the transmit SNR.

B. RIS-BS Channel Estimation

To examine the performance of RIS-BS channel reconstruction algorithm, the NMSE is utilized as the metric, defined as

$$\mathrm{NMSE}_{\mathrm{RB}} = \frac{\|\mathbf{H}_{\mathrm{RB}} - \tilde{\mathbf{H}}_{\mathrm{RB}}\|_F^2}{\|\mathbf{H}_{\mathrm{RB}}\|_F^2}. \tag{50}$$

Figure 10 presents the NMSE performance of the RIS-BS channel reconstruction versus the transmit SNR for a different number of active RIS and BS elements. We consider three setups of active RIS and BS elements: 1) setup 1: $N_{\mathrm{B}}^{\mathrm{UL}} = 32, N_{\mathrm{R}}^{\mathrm{DL}} = 32$, 2) setup 2: $N_{\mathrm{B}}^{\mathrm{UL}} = 128, N_{\mathrm{R}}^{\mathrm{DL}} = 64$, and 3) setup 3: $N_{\mathrm{B}}^{\mathrm{UL}} = 256, N_{\mathrm{R}}^{\mathrm{DL}} = 256$, while the traditional methods and the downlink training are also illustrated as benchmarks. The downlink training means that the BS sends downlink pilots to the RIS and the RIS-BS channel is reconstructed at the RIS side [43]. Moreover, in the downlink training, the near-field OMP algorithm with a pilot length 128 is adopted for estimating the RIS-BS channel. The near-field OMP algorithm is derived from [24], while the near-field codebook for UPA in [44] is also adopted.

By comparing the solid red curves, the solid blue curves and the green curves with triangles, it can be observed that the NMSE of the RIS-BS channel extrapolated from only 32 RIS elements and BS elements is close to the traditional schemes, which need to activate all RIS and BS elements. However, the overhead is only approximately $1/512$ of the traditional methods. Therefore, the high-dimensional double-side near-field channel can be reconstructed precisely at a low training overhead. Intuitively, if more training slots can be used for CSI acquisition, i.e., more active RIS elements, the accuracy of channel reconstruction is enhanced effectively. It can be concluded that the proposed scheme outperforms the benchmark downlink training under the same setup 3, while the training overhead of the proposed protocol is approximately 40, obviously lower than the benchmark with a pilot length 128. The comparisons validate the effectiveness of the proposed RIS structure and the proposed training protocol. Therefore, the proposed channel reconstruction scheme can simultaneously guarantee the requirements for timely and accurate channel reconstruction.

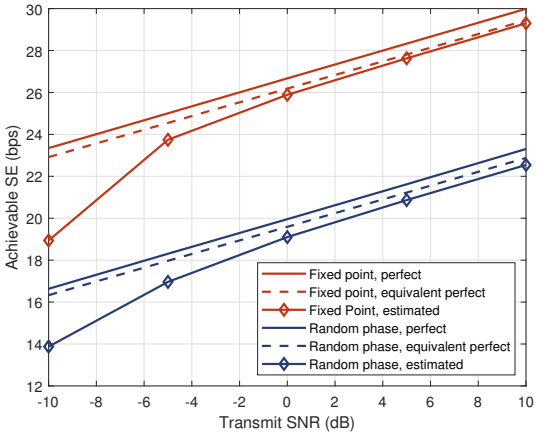

Fig. 11. The achievable SE versus the transmit SNR.

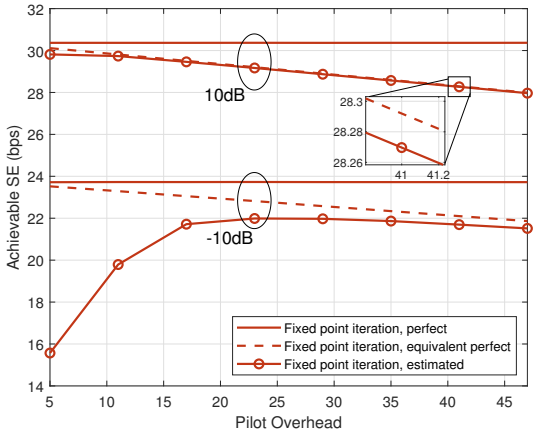

Fig. 12. The achievable SE versus the training overhead.

C. Achievable SE

The achievable SE is used to evaluate the effectiveness of the proposed channel reconstruction scheme and we consider the downlink data transmission for a single UE. Denoting the transmit signal of the BS as x, the signal received by the UE is $r = \sqrt{P}(\mathbf{h}_{\mathrm{UR}}^{\top}\boldsymbol{\Theta}\mathbf{H}_{\mathrm{RB}})\mathbf{f}x + n$, where $\mathbf{f} \in \mathbb{C}^{N_{\mathrm{B}}\times 1}$ is the equivalent BF vector[7] of the BS and n is the AWGN.

In this paper, we adopt the Fixed Point Iteration algorithm [45] to obtain the optimal phase of RIS. Afterwards, we derive the optimal BF vector $\mathbf{f}^{\star}$ under fully-digital assumption, and the analog BF matrix $\mathbf{F}_{\mathrm{RF}}^{\star} \in \mathbb{C}^{N_{\mathrm{B}}\times N_{\mathrm{RF,B}}}$ is [46]

$$\mathbf{F}_{\mathrm{RF}}^{\star} = \mathrm{blkdiag}(\mathbf{f}_{\mathrm{RF},1}, \mathbf{f}_{\mathrm{RF},2}, ..., \mathbf{f}_{\mathrm{RF},N_{\mathrm{RF,B}}}), \tag{51}$$

where $\mathbf{f}_{\mathrm{RF},n} = \exp(\jmath\angle[\mathbf{f}^{\star}]_{(n-1)N_{\mathrm{B}}/N_{\mathrm{RF,B}}+1:nN_{\mathrm{B}}/N_{\mathrm{RF,B}}})$ for $n = 1, ..., N_{\mathrm{RF,B}}$. Then, the digital BF vector is $\mathbf{f}_{\mathrm{BB}}^{\star} = {\mathbf{F}_{\mathrm{RF}}^{\star}}^{\dagger}\mathbf{f}^{\star}$. Therefore, the achievable SE is calculated as [47]

$$R = \frac{T_{\mathrm{c}} - T_{\mathrm{p}}}{T_{\mathrm{c}}} \log_2\left(1 + \frac{P}{\sigma_n^2}\left|(\mathbf{h}_{\mathrm{UR}}^{\top}\boldsymbol{\Theta}\mathbf{H}_{\mathrm{RB}})\mathbf{F}_{\mathrm{RF}}^{\star}\mathbf{f}_{\mathrm{BB}}^{\star}\right|^2\right). \tag{52}$$

In accordance with (52), we calculate the achievable SE based on perfect CSI and reconstructed CSI, denoted as $R^{\star}$ and R, respectively. We also introduce the equivalent achievable SE, denoted as $\tilde{R}$, which is calculated based on perfect CSI and the training overhead, i.e., $\tilde{R} = \frac{T_{\mathrm{c}}-T_{\mathrm{p}}}{T_{\mathrm{c}}}R^{\star}$.

Figure 11 compares the achievable SE derived by acquiring perfect CSI and reconstructed CSI under the Fixed Point Iteration strategy. We set the numbers of active RIS elements and BS elements as: $N_{\mathrm{R}}^{\mathrm{UL}} = 64$, $N_{\mathrm{B}}^{\mathrm{UL}} = 64$, and $N_{\mathrm{R}}^{\mathrm{DL}} = 64$. The solid curves represent the achievable SE calculated by perfect CSI and $T_{\mathrm{p}} = 0$, while the dotted curves represent the achievable SE calculated by perfect CSI and real T_{p}. By comparing the dotted curves with the solid curves with diamonds, it can be observed that the BF with the proposed channel reconstruction scheme yields comparable achievable SE with the perfect CSI. The performance gaps between solid curves with diamonds and solid curves without diamonds stems from the training overhead, which can be narrowed by activating less RIS/BS elements.

Figure 12 compares the achievable SE against the pilot overhead when the transmit SNR is -10 dB and 10 dB, respectively. When the SNR is low, the achievable SE first increases but then decreases. This is because the improvement of achievable SE caused by the accuracy boost of channel reconstruction cannot compensate for the degradation caused by the additional training overhead. However, when the SNR is high, the achievable SE decreases with the increase of training overhead, which means that the accuracy of reconstructed channel with low overhead is sufficient for data transmission. As shown in Fig. 12, the gaps between the curves with circles and the dotted curves are negligible, which means the proposed channel reconstruction scheme returns comparable SE with the perfect CSI case, even if a small portion of RIS elements and BS elements are activated.

VI. Conclusion

We proposed a switch-based sensing RIS structure that enables active elements' switching. To illustrate the advantages of this sensing RIS, we made a comprehensive analysis and comparison with different RIS structures from the perspective of CSI acquisition. Based on the proposed sensing RIS structure, we developed a novel CSI acquisition procedure that obtains the separate CSI accurately with low training overhead. Moreover, we considered the near-field UE-RIS channel and RIS-BS channel alike in our model, which is also compatible with far-field conditions. Afterwards, the RIS pattern activation strategy and training overhead were analyzed. Our numerical results demonstrated that the proposed scheme can realize accurate channel reconstruction, as well as enhanced SE.

Appendix A
Proof of Proposition 1

Assuming the angles θ and ϕ are perfectly matched, the radiation pattern w.r.t. the distance under a full RIS pattern, i.e., $G_{\mathrm{full}}(d_i)$, is written as (53). Denoting $\Delta d = \frac{1}{d_i} - \frac{1}{d}$, and $X_n = e^{\jmath\pi\Delta d\left(y_{n_h}^2 + z_{n_v}^2 - (y_{n_h}\sin\theta\sin\phi + z_{n_v}\cos\theta)^2\right)}$, based on the

[7]Due to the limitation of hybrid BF structure at the BS, we first consider the fully-digital structure of the BS and then derive the near-optimal analog BF matrix and digital BF vector for simplicity.

$$G_{\text{full}}(d_i) \approx \frac{1}{N_{\text{R}}} \left| \sum_{n_h=-(N_{\text{R}h}-1)/2}^{(N_{\text{R}h}-1)/2} \sum_{n_v=-(N_{\text{R}v}-1)/2}^{(N_{\text{R}v}-1)/2} \exp\left(\jmath\pi d_a^2 \left(\frac{1}{d_i} - \frac{1}{\ddot{d}} \right) \left(n_h^2 + n_v^2 - (n_h \sin\theta \sin\phi + n_v \cos\theta)^2 \right) \right) \right|$$
$$\approx \frac{1}{N_{\text{R}}} \left| \int_{-\frac{N_{\text{R}h}}{2}}^{\frac{N_{\text{R}h}}{2}} \int_{-\frac{N_{\text{R}v}}{2}}^{\frac{N_{\text{R}v}}{2}} \exp\left(\jmath\pi d_a^2 \left(\frac{1}{d_i} - \frac{1}{\ddot{d}} \right) \left(y^2 + z^2 - (y \sin\theta \sin\phi + z \cos\theta)^2 \right) \right) \mathrm{d}z\mathrm{d}y \right| \tag{53}$$

$$|\bar{X}_n| \approx \left| \frac{1}{N_{\text{R}}^{\text{act}}} \sum_{n \in \mathcal{N}_{\text{R}}^{\text{act}}} X_n \right| \approx \left| N_{\text{R}}^{\text{act}} \frac{1}{N_{\text{R}}^{\text{act}}} \int_{\frac{-N_{\text{R}h}}{2}}^{\frac{N_{\text{R}h}}{2}} \int_{\frac{-N_{\text{R}v}}{2}}^{\frac{N_{\text{R}v}}{2}} g(y_n, z_n) X_n \mathrm{d}z_n \mathrm{d}y_n \right| = \frac{1}{N_{\text{R}}} \left| \int_{\frac{-N_{\text{R}h}}{2}}^{\frac{N_{\text{R}h}}{2}} \int_{\frac{-N_{\text{R}v}}{2}}^{\frac{N_{\text{R}v}}{2}} X_n \mathrm{d}z_n \mathrm{d}y_n \right|. \tag{54}$$

weak law of large numbers, we obtain $\frac{\sum_{n \in \mathcal{N}_{\text{R}}^{\text{act}}} X_n}{N_{\text{R}}^{\text{act}}} \to \bar{X}_n$, where $\bar{X}_n$ is the mean of X_n. Taking the modulus of both sides, we obtain $\frac{|\sum_{n \in \mathcal{N}_{\text{R}}^{\text{act}}} X_n|}{N_{\text{R}}^{\text{act}}} \approx |\bar{X}_n|$. We now assume that the positions of the RIS elements, $(y_n, z_n), n = 1, ..., N_{\text{R}}^{\text{act}}$ are continuous random variables and follow the uniform distribution independently, i.e. $y_n \sim \mathcal{U}(-\frac{N_{\text{R}h}}{2}, \frac{N_{\text{R}h}}{2})$ and $z_n \sim \mathcal{U}(-\frac{N_{\text{R}v}}{2}, \frac{N_{\text{R}v}}{2})$, respectively. Therefore, the jointly probability density function (PDF) is $g(y_n, z_n) = \frac{1}{N_{\text{R}h}} \frac{1}{N_{\text{R}v}} = \frac{1}{N_{\text{R}}}$ and $|\bar{X}_n|$ is denoted as (54) [39]. Considering $N_{\text{R}}^{\text{act}}$ is constant, one RIS element's activation, i.e. $\mathbf{W}_{\text{R}}^{\text{act}}$, can be considered as a random trial. Then, by taking the expectation of $G(d_i)$ w.r.t. $\mathbf{W}_{\text{R}}^{\text{act}}$, we deduce

$$\mathbb{E}_{\mathbf{W}_{\text{R}}^{\text{act}}}\{G(d_i)\} \approx \mathbb{E}\left\{ \left| \frac{\sum_{n \in \mathcal{N}_{\text{R}}^{\text{act}}} X_n}{N_{\text{R}}^{\text{act}}} \right| \right\} \approx \mathbb{E}\{|\bar{X}_n|\} = |\bar{X}_n| = G_{\text{full}}(d_i). \tag{55}$$

Appendix B
Proof of Proposition 2

We rewrite the signal model of the RIS as follows

$$\dot{\mathbf{y}} = \dot{\mathbf{W}}_{\text{R}} \mathbf{h} + \mathbf{n}, \tag{56}$$

where $\dot{\mathbf{W}}_{\text{R}} \in \{0,1\}^{N_{\text{R}} \times N_{\text{R}}}$ is a diagonal matrix whose n-th diagonal element represents that the n-th element is active if $[\dot{\mathbf{W}}_{\text{R}}]_{n,n} = 1$. Note that (56) is equal to (15) by removing the zeros elements of $\dot{\mathbf{y}}$ and zeros rows of $\dot{\mathbf{W}}_{\text{R}}$, respectively. Assuming that $N_{\text{R}}^{\text{act}}$ elements are active, $\dot{\mathbf{W}}_{\text{R}}$ satisfies $\dot{\mathbf{W}}_{\text{R}}^{\text{H}} \dot{\mathbf{W}}_{\text{R}} = \dot{\mathbf{W}}_{\text{R}}$ and $\mathbb{E}\{\dot{\mathbf{W}}_{\text{R}}^{\text{H}} \dot{\mathbf{W}}_{\text{R}}\} = \frac{N_{\text{R}}^{\text{act}}}{N} \mathbf{I}_{N_{\text{R}} \times N_{\text{R}}}$. Therefore, the expectation of the FIM $\dot{\mathbf{F}}(\boldsymbol{\varpi})$, derived by $N_{\text{R}}^{\text{act}}$ active elements, satisfies $\mathbb{E}\{\dot{\mathbf{F}}(\boldsymbol{\varpi})\} = \frac{N_{\text{R}}^{\text{act}}}{N_{\text{R}}} \mathbf{F}_{\text{full}}(\boldsymbol{\varpi})$. Since the non-diagonal elements of $\dot{\mathbf{F}}(\boldsymbol{\varpi})$ and $\mathbf{F}_{\text{full}}(\boldsymbol{\varpi})$ are relatively small compared to the diagonal elements, $\dot{\mathbf{F}}(\boldsymbol{\varpi})$ and $\mathbf{F}_{\text{full}}(\boldsymbol{\varpi})$ can be approximated as diagonal matrices. Based on the approximation $\mathbb{E}\{\frac{1}{X}\} \approx \frac{1}{\mathbb{E}\{X\}}$ [48], where X is a random variable, we can obtain $\mathbb{E}\{\mathbf{F}^{-1}\} \approx \mathbb{E}\{\mathbf{F}\}^{-1}$, where $\mathbf{F} \in \{\dot{\mathbf{F}}, \mathbf{F}_{\text{full}}\}$. Then, the expectation of the CRLB w.r.t. the i-th parameter x, $x \in \{d, \theta, \phi\}$, $i = 1, 2, 3$, is derived as

$$\mathbb{E}\{\text{CRLB}_x\} = \sum_{l=1}^{L} [\mathbb{E}\{\dot{\mathbf{F}}^{-1}(\boldsymbol{\varpi})\}]_{3(l-1)+i, 3(l-1)+i}$$
$$\approx \sum_{l=1}^{L} [\mathbb{E}\{\dot{\mathbf{F}}\}^{-1}(\boldsymbol{\varpi})]_{3(l-1)+i, 3(l-1)+i} \approx \frac{N_{\text{R}}}{N_{\text{R}}^{\text{act}}} \text{CRLB}_{x,\text{full}}. \tag{57}$$

References

[1] M. Matthaiou *et al.*, "The road to 6G: Ten physical layer challenges for communications engineers," *IEEE Commun. Mag.*, vol. 59, no. 1, pp. 64-69, Jan. 2021.

[2] J. Zhang, E. Björnson, M. Matthaiou, D. W. K. Ng, H. Yang, and D. J. Love, "Prospective multiple antenna technologies for beyond 5G," *IEEE J. Sel. Areas Commun.*, vol. 38, no. 8, pp. 1637–1660, Aug. 2020.

[3] Y. Han, W. Tang, S. Jin, C. -K. Wen, and X. Ma, "Large intelligent surface-assisted wireless communication exploiting statistical CSI," *IEEE Trans. Veh. Technol.*, vol. 68, no. 8, pp. 8238-8242, Aug. 2019.

[4] Q. Wu and R. Zhang, "Intelligent reflecting surface enhanced wireless network via joint active and passive beamforming," *IEEE Trans. Wireless Commun.*, vol. 18, no. 11, pp. 5394–5409, Nov. 2019.

[5] M. D. Renzo *et al.*, "Smart radio environments empowered by reconfigurable intelligent surfaces: How it works, state of research, and the road ahead," *IEEE J. Sel. Areas Commun.*, vol. 38, no. 11, pp. 2450–2525, Nov. 2020.

[6] J. Sang *et al.*, "Multi-scenario broadband channel measurement and modeling for sub-6 GHz RIS-assisted wireless communication systems," *IEEE Trans. Wireless Commun.*, early access, doi: 10.1109/TWC.2023.3330977.

[7] J. Sang *et al.*, "Coverage enhancement by deploying RIS in 5G commercial mobile networks: Field trials," *IEEE Wireless Commun.*, vol. 31, no. 1, pp. 172-180, Feb. 2024.

[8] C. Huang, A. Zappone, G. C. Alexandropoulos, M. Debbah, and C. Yuen, "Reconfigurable intelligent surfaces for energy efficiency in wireless communication," *IEEE Trans. Wireless Commun.*, vol. 18, no. 8, pp. 4157–4170, Aug. 2019.

[9] K. Feng, X. Li, Y. Han, and Y.-J. Chen, "Joint beamforming optimization for reconfigurable intelligent surface-enabled MISO-OFDM systems," *China Commun.*, vol. 18, no. 3, pp. 63-79, Mar. 2021.

[10] K. Feng, Q. Wang, X. Li, and C.-K. Wen, "Deep reinforcement learning based intelligent reflecting surface optimization for MISO communication systems," *IEEE Wireless Commun. Lett.*, vol. 9, no. 5, pp. 745-749, May 2020.

[11] P. Chen, W. Huang, X. Li, and S. Jin, "Deep reinforcement learning based power Minimization for RIS-assisted MISO-OFDM systems," *China Commun.*, vol. 20, no. 4, pp. 259-269, Apr. 2023.

[12] Z. Abu-Shaban *et al.*, "Near-field localization with a reconfigurable intelligent surface acting as lens," in *Proc. IEEE ICC*, Jun. 2021, pp. 1-6.

[13] Y. Han, S. Jin, C. -K. Wen, and T. Q. S. Quek, "Localization and channel reconstruction for extra large RIS-assisted massive MIMO systems," *IEEE J. Sel. Top. Signal Proces.*, vol. 16, no. 5, pp. 1011-1025, Aug. 2022.

[14] A. L. Swindlehurst, G. Zhou, R. Liu, C. Pan, and M. Li, "Channel estimation with reconfigurable intelligent surfaces—A general framework," *Proc. IEEE*, vol. 110, no. 9, pp. 1312-1338, Sept. 2022.

[15] L. Wei, C. Huang, G. C. Alexandropoulos, and C. Yuen, "Parallel factor decomposition channel estimation in RIS-assisted multi-user MISO communication," in *Proc. IEEE SAM*, 2020, pp. 1–5.

[16] J. He, H. Wymeersch, and M. Juntti, "Channel estimation for RIS-aided mmWave MIMO systems via atomic norm minimization," *IEEE Trans. Wireless Commun.*, vol. 20, no. 9, pp. 5786-5797, Sept. 2021.

[17] A. Taha, M. Alrabeiah, and A. Alkhateeb, "Enabling large intelligent surfaces with compressive sensing and deep learning," *IEEE Access*, vol. 9, pp. 44304-44321, 2021.

[18] G. C. Alexandropoulos and E. Vlachos, "A hardware architecture for reconfigurable intelligent surfaces with minimal active elements for explicit channel estimation," in *Proc. IEEE ICASSP*, May 2020, pp. 9175-9179.
[19] Y. Lin, S. Jin, M. Matthaiou, and X. You, "Tensor-based algebraic channel estimation for hybrid IRS-assisted MIMO-OFDM," *IEEE Trans. Wireless Commun.*, vol. 20, no. 6, pp. 3770-3784, Jun. 2021.
[20] R. Schroeder, J. He, and M. Juntti, "Passive RIS vs. hybrid RIS: A comparative study on channel estimation," in *Proc. IEEE VTC*, Apr. 2021, pp. 1-7.
[21] R. Schroeder, J. He, G. Brante, and M. Juntti, "Two-stage channel estimation for hybrid RIS assisted MIMO systems," *IEEE Trans. Commun.*, vol. 70, no. 7, pp. 4793-4806, Jul. 2022.
[22] S. Yang, W. Lyu, D. Wang, and Z. Zhang, "Separate channel estimation with hybrid RIS-aided multi-user communications," *IEEE Trans. Veh. Technol.*, vol. 72, no. 1, pp. 1318-1324, Jan. 2023.
[23] S. Yang, W. Lyu, Z. Hu, Z. Zhang, and C. Yuen, "Channel estimation for near-field XL-RIS-aided mmwave hybrid beamforming architectures," *IEEE Trans. Veh. Technol.*, early access, doi: 10.1109/TVT.2023.3261340.
[24] Y. Lu and L. Dai, "Near-field channel estimation in mixed LoS/NLoS environments for extremely large-scale MIMO systems," *IEEE Trans. Commun.*, vol. 71, no. 6, pp. 3694-3707, Jun. 2023.
[25] B. Mamandipoor, D. Ramasamy, and U. Madhow, "Newtonized orthogonal matching pursuit: Frequency estimation over the continuum," *IEEE Trans. Signal Proces.*, vol. 64, no. 19, pp. 5066-5081, Oct. 2016.
[26] S. Park, A. Alkhateeb, and R. W. Heath Jr., "Dynamic subarrays for hybrid precoding in wideband mmWave MIMO systems," *IEEE Trans. Wireless Commun.*, vol. 16, no. 5, pp. 2907-2920, May 2017.
[27] S. Payami, N. Mysore Balasubramanya, C. Masouros, and M. Sellathurai, "Phase shifters versus switches: An energy efficiency perspective on hybrid beamforming," *IEEE Wireless Commun. Lett.*, vol. 8, no. 1, pp. 13-16, Feb. 2019.
[28] A. M. Sayeed, "Deconstructing multiantenna fading channels," *IEEE Trans. Signal Process.*, vol. 50, no. 10, pp. 2563-2579, Oct. 2002.
[29] K. T. Selvan and R. Janaswamy, "Fraunhofer and fresnel distances: Unified derivation for aperture antennas," *IEEE Antennas Propag. Mag.*, vol. 59, no. 4, pp. 12-15, Aug. 2017.
[30] Y. Han, W. Tang, X. Li, M. Matthaiou, and S. Jin, "CSI acquisition in RIS-assisted mobile communication systems," *National Science Review*, Volume 10, Issue 8, nwad127, Aug. 2023.
[31] G. Lee, H. Lee, J. Oh, J. Chung, and J. Choi, "Channel estimation for reconfigurable intelligent surface with a few active elements," *IEEE Trans. Veh. Technol.*, vol. 72, no. 6, pp. 8170-8174, Jun. 2023.
[32] J. Wang *et al.*, "Reconfigurable intelligent surface: Power consumption modeling and practical measurement validation," *IEEE Trans. Commun.*, early access, doi: 10.1109/TCOMM.2024.3382332.
[33] C. Hu, L. Dai, S. Han, and X. Wang, "Two-timescale channel estimation for reconfigurable intelligent surface aided wireless communications," *IEEE Trans. Commun.*, vol. 69, no. 11, pp. 7736-7747, Nov. 2021.
[34] X. Yang, S. Jin, G. Y. Li, and X. Li, "Asymmetrical uplink and downlink transceivers in massive MIMO systems," *IEEE Trans. Veh. Technol.*, vol. 70, no. 11, pp. 11632-11647, Nov. 2021.
[35] H. Miao *et al.*, "Sub-6 GHz to mmWave for 5G-advanced and beyond: Channel measurements, characteristics and impact on system performance," *IEEE J. Sel. Areas Commun.*, vol. 41, no. 6, pp. 1945-1960, Jun. 2023.
[36] Y. Han, S. Jin, X. Li, C. -K. Wen, and T. Q. S. Quek, "Multi-domain channel extrapolation for FDD massive MIMO systems," *IEEE Trans. Commun.*, vol. 69, no. 12, pp. 8534-8550, Dec. 2021.
[37] C. -L. Liu and P. P. Vaidyanathan, "Super nested arrays: Linear sparse arrays with reduced mutual coupling — part I: Fundamentals," *IEEE Trans. Signal Process.*, vol. 64, no. 15, pp. 3997-4012, Aug., 2016.
[38] C. -L. Liu and P. P. Vaidyanathan, "Hourglass arrays and other novel 2-D sparse arrays with reduced mutual coupling," *IEEE Trans. Signal Process.*, vol. 65, no. 13, pp. 3369-3383, Jul. 2017.
[39] Y. Lo, "A mathematical theory of antenna arrays with randomly spaced elements," *IEEE Trans. Antennas Propagat.*, vol. 12, no. 3, pp. 257-268, May 1964.
[40] S. M. Kay, *Fundamentals of Statistical Processing: Estimation Theory.* Englewood Cliffs, NJ, USA: Prentice-Hall, 1993.
[41] Y. Han, T. -H. Hsu, C. -K. Wen, K. -K. Wong, and S. Jin, "Efficient downlink channel reconstruction for FDD multi-antenna systems," *IEEE Trans. Wireless Commun.*, vol. 18, no. 6, pp. 3161-3176, Jun. 2019.
[42] J. Lee, G. -T. Gil, and Y. H. Lee, "Channel estimation via orthogonal matching pursuit for hybrid MIMO systems in millimeter wave communications," *IEEE Trans. Commun.*, vol. 64, no. 6, pp. 2370-2386, Jun. 2016.
[43] R. Schroeder, J. He, and M. Juntti, "Passive RIS vs. hybrid RIS: A comparative study on channel estimation," in *Proc. IEEE VTC*, Apr. 2021, pp. 1-7.
[44] Z. Wu and L. Dai, "Multiple access for near-field communications: SDMA or LDMA?," *IEEE J. Sel. Areas Commun.*, vol. 41, no. 6, pp. 1918-1935, Jun. 2023.
[45] X. Yu, D. Xu, and R. Schober, "MISO wireless communication systems via intelligent reflecting surfaces," in *Proc. IEEE/CIC ICCC*, Aug. 2019, pp. 735-740.
[46] J. Tian, Y. Han, S. Jin, and M. Matthaiou, "Low-overhead localization and VR identification for subarray-based ELAA systems," *IEEE Wireless Commun. Lett.*, vol. 12, no. 5, pp. 784-788, May 2023.
[47] H. Q. Ngo, E. G. Larsson, and T. L. Marzetta, "Energy and spectral efficiency of very large multiuser MIMO systems," *IEEE Trans. Commun.*, vol. 61, no. 4, pp. 1436-1449, Apr. 2013.
[48] X. Gao, M. Sitharam, and A. E. Roitberg, "Bounds on the Jensen gap, and implications for mean-concentrated distributions," Aug. 2020, *arXiv:1712.05267v5*.

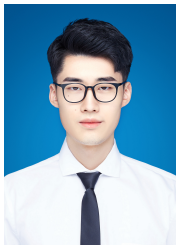

Jiachen Tian (Graduate Student Member, IEEE) received the B.S. degree from Southeast University, Nanjing, China, in 2022. He is currently working towards the Ph.D. degree with the School of Information Science and Engineering, Southeast University. His research interests include extra large-scale MIMO and reconfigurable intelligent surfaces.

Yu Han (Member, IEEE) received the B.S. degree in communications engineering from Hangzhou Dianzi University, Hangzhou, China, in 2012, and the M.S. and Ph.D. degrees in information and communications engineering from Southeast University, Nanjing, China, in 2015 and 2020, respectively. She was a Post-Doctoral Fellow with the Singapore University of Technology and Design, Singapore, till 2020. She is currently an Associate Professor with Southeast University, Nanjing, China. Her research interests include extra large-scale MIMO and reconfigurable intelligent surface. Dr. Han and her coauthors have been awarded the IEEE Vehicular Technology Society 2023 Jack Neubauer Memorial Award.

Shi Jin (Fellow, IEEE) received the B.S. degree in communications engineering from Guilin University of Electronic Technology, Guilin, China, in 1996, the M.S. degree from Nanjing University of Posts and Telecommunications, Nanjing, China, in 2003, and the Ph.D. degree in information and communications engineering from the Southeast University, Nanjing, in 2007. From June 2007 to October 2009, he was a Research Fellow with the Adastral Park Research Campus, University College London, London, U.K. He is currently with the faculty of the National Mobile Communications Research Laboratory, Southeast University. His research interests include wireless communications, random matrix theory, and information theory. He is serving as an Area Editor for the Transactions on Communications and IET Electronics Letters. He was an Associate Editor for the IEEE Transactions on Wireless Communications, and IEEE Communications Letters, and IET Communications. Dr. Jin and his coauthors have been awarded the 2011 IEEE Communications Society Stephen O. Rice Prize Paper Award in the field of communication theory, the IEEE Vehicular Technology Society 2023 Jack Neubauer Memorial Award, a 2022 Best Paper Award and a 2010 Young Author Best Paper Award by the IEEE Signal Processing Society.

Xiao Li (Member, IEEE) received the Ph.D. degree in communication and information systems from Southeast University, Nanjing, China, in 2010. She then joined the School of Information Science and Engineering, Southeast University, where she has been a Professor in information systems and communications since July 2020. From January 2013 to January 2014, she was a Postdoctoral Fellow at The University of Texas at Austin, Austin, TX, USA. Her current research interests include massive MIMO, Reconfigurable intelligent surface assisted communications, and intelligent communications. Dr. Li was a recipient of the 2013 National Excellent Doctoral Dissertation of China for her Ph.D. dissertation. She serves as an Associate Editor for the IEEE Transactions on Wireless Communications, the IEEE Wireless Communications Letters, and the Electronics Letters, and a Guest Editor for the Digital Communications and Networks.

Jun Zhang (Senior Member, IEEE) received the M.S. degree in Statistics with Department of Mathematics from Southeast University, Nanjing, China, in 2009, and the Ph.D. degree in Communications Information System with the National Mobile Communications Research Laboratory, Southeast University, Nanjing, China, in 2013. From 2013 to 2015, he was a Postdoctoral Research Fellow with Singapore University of Technology and Design, Singapore. Since 2015, he is with the faculty of the Jiangsu Key Laboratory of Wireless Communications, College of Telecommunications and Information Engineering, Nanjing University of Posts and Telecommunications, where he is currently a Professor. His research interests include massive MIMO communications, RIS-assisted wireless communications, UAV-assisted wireless communications, physical layer security, and large dimensional random matrix theory. Dr. Zhang was a recipient of the Globcom Best Paper Award in 2016, the IEEE APCC Best Paper Award in 2017, the IEEE JC&S Best Paper Award in 2022, the IEEE/CIC ICCC Best Paper Award in 2023, and the WCSP Best Paper Award in 2023. He has served as an Associate Editor for the IEEE Communications Letters.

Michail Matthaiou (Fellow, IEEE) was born in Thessaloniki, Greece in 1981. He obtained the Diploma degree (5 years) in Electrical and Computer Engineering from the Aristotle University of Thessaloniki, Greece in 2004. He then received the M.Sc. (with distinction) in Communication Systems and Signal Processing from the University of Bristol, U.K. and Ph.D. degrees from the University of Edinburgh, U.K. in 2005 and 2008, respectively. From September 2008 through May 2010, he was with the Institute for Circuit Theory and Signal Processing, Munich University of Technology (TUM), Germany working as a Postdoctoral Research Associate. He is currently a Professor of Communications Engineering and Signal Processing and Deputy Director of the Centre for Wireless Innovation (CWI) at Queen's University Belfast, U.K. after holding an Assistant Professor position at Chalmers University of Technology, Sweden. His research interests span signal processing for wireless communications, beyond massive MIMO, intelligent reflecting surfaces, mm-wave/THz systems and deep learning for communications.

Dr. Matthaiou and his coauthors received the IEEE Communications Society (ComSoc) Leonard G. Abraham Prize in 2017. He currently holds the ERC Consolidator Grant BEATRICE (2021-2026) focused on the interface between information and electromagnetic theories. To date, he has received the prestigious 2023 Argo Network Innovation Award, the 2019 EURASIP Early Career Award and the 2018/2019 Royal Academy of Engineering/The Leverhulme Trust Senior Research Fellowship. His team was also the Grand Winner of the 2019 Mobile World Congress Challenge. He was the recipient of the 2011 IEEE ComSoc Best Young Researcher Award for the Europe, Middle East and Africa Region and a co-recipient of the 2006 IEEE Communications Chapter Project Prize for the best M.Sc. dissertation in the area of communications. He has co-authored papers that received best paper awards at the 2018 IEEE WCSP and 2014 IEEE ICC. In 2014, he received the Research Fund for International Young Scientists from the National Natural Science Foundation of China. He is currently the Editor-in-Chief of Elsevier Physical Communication, a Senior Editor for IEEE WIRELESS COMMUNICATIONS LETTERS and IEEE SIGNAL PROCESSING MAGAZINE, and an Associate Editor for IEEE TRANSACTIONS ON COMMUNICATIONS. He is an IEEE Fellow.